

Searching for eV-mass Axion-like Particles with Cross Correlations between Line Intensity and Weak Lensing Maps

Masato Shirasaki^{1,2,*}

¹*National Astronomical Observatory of Japan (NAOJ), Mitaka, Tokyo 181-8588, Japan*

²*The Institute of Statistical Mathematics, Tachikawa, Tokyo 190-8562, Japan*

(Dated: May 3, 2021)

We study cross correlations between line intensity and weak lensing maps to search for axion-like particles (ALPs). Radiative decay of eV-mass ALPs can contribute to cosmic background emissions at optical and infrared wavelengths. Line intensity mapping is a unique means of measuring the background emission at a given photon frequency. If ALPs constitute the abundance of cosmic dark matter, line intensity maps can correlate with large-scale structures probed by weak gravitational lensing effects in galaxy imaging surveys. We develop a theoretical framework to predict the cross correlation. We then explore potentiality of probing ALPs with the cross correlation in upcoming galaxy-imaging and spectral surveys. Assuming SPHEREx and the Vera Rubin Observatory's Legacy Survey of Space and Time (LSST), we find that the cross correlation by the ALP decay can be greater than the astrophysical-line counterparts at wavelength of ~ 3000 nm for ALPs with a particle mass of $m_a \sim 1$ eV and a particle-to-two-photons coupling of $g_{a\gamma\gamma} \sim 1 \times 10^{-11} \text{ GeV}^{-1}$. We also predict that a null detection of the cross correlation can place a 2σ -level upper bound of $g_{a\gamma\gamma} \lesssim 10^{-11} \text{ GeV}^{-1}$ for eV-mass ALPs, improving the current constraint by a factor of ~ 10 . We then make a forecast of expected constraints on ALP parameters in SPHEREx and LSST by Fisher analysis, providing a guideline of searching for the ALP decay with the large-scale structure data.

I. INTRODUCTION

The nature of cosmic dark matter is one of the long-standing mysteries in modern astronomy and physics. Dark matter accounts for about 80% of the average mass density in our universe [1], but can not be explained by the Standard Model of particle physics. The QCD axion is a well-motivated candidate of dark matter [2–4], while it is originally proposed as a solution to the strong CP problem [5–8]. The QCD axion is a pseudoscalar boson with an approximate shift symmetry. More general light pseudoscalars are known as axion-like particles, or ALPs. ALPs are pseudo-Nambu Goldstone bosons produced through the breaking of global $U(1)$ symmetries, or zero modes of higher dimensional gauge fields [9–12]. Because ALPs are not associated with the strong CP problem, they can exhibit a wider range of couplings and masses. Hence, ALPs are considered to be a compelling candidate of dark matter [13].

In this paper, we are interested in the search for ALPs with astronomical datasets. In particular, we pay special attention to radiative decay of ALPs with their particle mass of about 1 eV. The eV-mass ALPs can decay into two photons with photon frequencies of $\sim 10^{14}$ Hz, corresponding to optical and infrared wavelengths. Galaxy surveys at optical and infrared bands are about to reach their peak. Upcoming large surveys include the Vera Rubin Observatory's Legacy Survey of Space and Time (LSST)¹, The Nancy Roman Space Telescope², Euclid³,

and SPHEREx⁴.

Among the upcoming surveys, SPHEREx provides a unique opportunity of studying cumulative background emissions at optical and infrared bands with line-intensity mapping techniques. The line-intensity mapping measures photon intensity at a narrow range of frequency along a given line-of-sight direction, allowing us to explore faint astrophysical sources that are difficult to be detected individually. If a fraction of cosmic dark matter would consist of eV-mass ALPs, ALP-decay photons contribute to the line intensity maps obtained by SPHEREx. At the same time, ALPs are at work as building blocks of large-scale structures in the universe and they distort shapes of distant galaxies by weak gravitational lensing effects (see, e.g. Ref. [14] for a review). Hence, ALPs can affect two different observables of line intensity maps and weak lensing effects, introducing spatial cross correlations between the two. Weak gravitational lensing effects are now recognized as a main science driver in galaxy imaging surveys and most upcoming imaging surveys are aimed at measuring the effects with unprecedented accuracy. It is thus strongly motivated to study expected cross correlations between the line intensity maps and weak lensing effects in galaxy imaging surveys for the search for ALPs, enhancing the science returns from large galaxy surveys.

It would be worth noting that Ref. [15] has already proposed the ALP search by using cross correlations between line intensity maps and other large-scale structure data. Nevertheless, they mainly focus on a biased tracer of large scale structures such as galaxies, while we

* masato.shirasaki@nao.ac.jp

¹ <https://www.lsst.org/>

² <https://roman.gsfc.nasa.gov/>

³ <https://sci.esa.int/web/euclid>

⁴ <https://www.jpl.nasa.gov/missions/spherex/>

consider the weak lensing effects to extract unbiased information about underlying cosmic mass density fields. We also study possible astrophysical contributions to the cross correlation analysis, which are ignored in Ref. [15]. Recently, Ref. [16] proposed a statistical approach to constrain decaying dark matter with line-intensity maps alone. They studied a joint analysis of auto correlation functions and one-point probability distributions in line intensity maps. Our approach is thought to be complementary to that in Ref. [16].

The rest of the present paper is organized as follows. In Section II, we describe observables of interest and relevant physical effects to the observables. In Section III, we summarize a theoretical model to predict cross correlation functions between line intensity maps and weak lensing effects in galaxy shapes. We present the results in Section IV. Concluding remarks and discussions are given in Section V. Throughout, we consider a flat universe with the standard cosmological parameters $H_0 = 100 h \text{ km s}^{-1}$ with $h = 0.68$, the average matter density $\Omega_{\text{m}0} = 0.315$, the baryon density $\Omega_{\text{b}0} = 0.0491$, the cosmological constant $\Omega_{\Lambda} = 0.685$, the spectral index of initial curvature fluctuations $n_s = 0.97$, and the amplitude of matter density fluctuations within $8 h^{-1} \text{ Mpc}$, $\sigma_8 = 0.83$. Note that we adopt natural units with $c = \hbar = 1$, where c is the speed of light and \hbar is the reduced Planck constant.

II. OBSERVABLES

In this section, we introduce two observables of interest, the line-intensity and weak-lensing maps. The former provides the cumulative emission from sources fainter than detection limits in spectroscopic surveys, while the latter is the projected mass density distribution obtained in galaxy imaging surveys.

A. Line Intensity

The observed intensity I at photon frequency ν along a given direction $\boldsymbol{\theta}$ is expressed as

$$I(\boldsymbol{\theta} | \nu) = \frac{1}{4\pi} \int \frac{d\chi}{1+z} \epsilon(\mathbf{r}, \nu', z), \quad (1)$$

where $\nu' = \nu(1+z)$ is the photon frequency emitted at the source redshift z , χ is the comoving distance to the source, and $\epsilon(\mathbf{r}, \nu', z)$ represents the volume emissivity (i.e., the photon energy emitted per unit volume, time, and energy range) at the three-dimensional position of $\mathbf{r} = (\chi(z)\boldsymbol{\theta}, \chi(z))$ and the frequency ν' . Note that we define the volume emissivity in the comoving coordinate in Eq. (1). In line intensity mapping measurements, we are interested in any emission lines which can be observed at the frequency ν . Because the line width is usually negligible compared to the spectroscopic resolution in the

instrument⁵, we assume that the volume emissivity is given by

$$\epsilon(\mathbf{r}, \nu, z) = \rho_L(\mathbf{r}, z) \delta_{\text{D}}^{(1)}(\nu - \nu_0), \quad (2)$$

where ρ_L is the luminosity density of sources, $\delta_{\text{D}}^{(n)}$ is the n -dimensional Dirac delta function, ν_0 is the rest-frame line frequency of interest. Throughout this paper, we define the intensity in units of $\text{erg/s/cm}^2/\text{Hz/str}$. In the following, we briefly describe observable lines at optical and infrared bands, associated with the ALP decay and some relevant astrophysical sources.

1. ALP decay

Axion-like particles (ALPs) are light, weakly-interacting pseudo-scalar particles. A common feature among ALP models is that they can decay into photons with their decay rate Γ being

$$\Gamma = \frac{g_{a\gamma\gamma}^2 m_a^3}{64\pi} \quad (3)$$

$$= 7.556 \times 10^{-26} \text{ s}^{-1} \left(\frac{g_{a\gamma\gamma}}{10^{-10} \text{ GeV}^{-1}} \right)^2 \left(\frac{m_a}{1 \text{ eV}} \right)^3, \quad (4)$$

where m_a and $g_{a\gamma\gamma}$ are the mass and the particle-to-two-photon coupling constant of ALPs, respectively. In this decay, the emitted photon frequency is given by $\nu_a = m_a/(4\pi) = 1.21 \times 10^{14} \text{ Hz}$ ($m_a/1 \text{ eV}$).

Suppose that ALPs can constitute a part of dark matter, we can express the luminosity density due to the ALP decay as

$$\rho_{L,a}(\mathbf{r}, z) = \Gamma f_a \rho_{\text{DM}}(\mathbf{r}, z), \quad (5)$$

where f_a is the fraction of ALPs in the dark matter and $\rho_{\text{DM}}(\mathbf{r}, z)$ represents the dark matter density at redshift z . In the following, we consider the case of $f_a = 1$ for simplicity⁶. Using Eqs. (1), (2), and (5), one can find

$$I_a(\boldsymbol{\theta} | \nu) = \int d\chi W_{\text{DM}}(z|\nu) [1 + \delta_{\text{DM}}(\mathbf{r}, z)], \quad (6)$$

$$W_{\text{DM}}(z|\nu) = \frac{\Gamma}{4\pi} \frac{\Omega_{\text{DM}} \rho_{\text{crit},0}}{\nu_a H(z)} \delta_{\text{D}}^{(1)}(\chi - \chi_a), \quad (7)$$

where $\Omega_{\text{DM}} = \Omega_{\text{m}0} - \Omega_{\text{b}0} \sim 0.26$ is the dimensionless dark matter density, $\rho_{\text{crit},0}$ is the critical density at present, δ_{DM} is the dark matter density contrast, $H(z)$ is the Hubble expansion parameter at redshift z , χ_a is the comoving distance to the redshift z_a which is defined by $z_a \equiv \nu_a/\nu - 1$.

⁵ The virial velocity dispersion in typical galaxy-sized halos with $M = 10^{12-13} M_{\odot}$ can be estimated as $\sim 200 \text{ km/s}$. Hence, we can ignore the velocity dispersion effect in the analysis as long as setting the frequency resolution to $\lesssim 100$.

⁶ Our parameter forecasts can be easily generalized for $f_a < 1$ if one replaces $g_{a\gamma\gamma}$ with $g_{a\gamma\gamma} f_a^{1/2}$.

2. Astrophysical sources

The H_α line is a Balmer line that corresponds to a transition between energy levels $n = 3$ to $n = 2$ of neutral hydrogen. It is commonly used to study star-forming galaxies and quasars at $z \lesssim 2$ so far. The rest-frame wavelength of the H_α line is given by 656.28 nm, which is suitable for studying faint galaxies as well as diffuse emissions from intergalactic media in ongoing line-intensity mapping surveys.

It is known that the strength of the H_α line shows a tight correlation with the star-formation rate (SFR) of galaxies [17]. The commonly used relation between the SFR and the intrinsic H_α luminosity is provided as

$$L_{H_\alpha} = 1.26 \times 10^{41} \text{ (erg/s)} \left(\frac{\text{SFR}}{1 M_\odot/\text{yr}} \right), \quad (8)$$

where L_{H_α} is the intrinsic luminosity. The observed H_α luminosity $L_{H_\alpha}^{\text{obs}}$ is subject to dust extinction. We obtain the observed luminosity by accounting for the extinction with a magnitude of A_{H_α} ,

$$L_{H_\alpha}^{\text{obs}} = 10^{-A_{H_\alpha}/2.5} L_{H_\alpha}. \quad (9)$$

In this paper, we adopt $A_{H_\alpha} = 1$ mag which is a typical value in large H_α surveys [18].

To evaluate the H_α luminosity density, we assume that any star formation processes occur at the centers of single dark matter halos and SFRs can be determined by a function of halo masses and redshifts. In this halo-based model, we can express the H_α luminosity density ρ_{L,H_α} as

$$\rho_{L,H_\alpha}(\mathbf{r}, z) = \sum_i L_{H_\alpha}^{\text{obs}}(M_i, z) \delta_D^{(3)}(\mathbf{r} - \mathbf{r}_i) \quad (10)$$

$$= \mathcal{L}_{H_\alpha} \sum_i \dot{M}_*(M_i, z) \delta_D^{(3)}(\mathbf{r} - \mathbf{r}_i), \quad (11)$$

where \dot{M}_* is the SFR in units of M_\odot/yr , M_i and \mathbf{r}_i represent a halo mass and spatial coordinate of the i -th halo, the index i runs over all the halos at redshift z in a unit volume, and we introduce $\mathcal{L}_{H_\alpha} = 1.26 \times 10^{41} \text{ (erg/s)} \times 10^{-A_{H_\alpha}/2.5}$.

We start from computing the average luminosity density based on Eq. (10). It is given by

$$\bar{\rho}_{L,H_\alpha}(z) = 10^{-A_{H_\alpha}/2.5} \int dL_{H_\alpha} \frac{dn}{dL_{H_\alpha}} L_{H_\alpha}, \quad (12)$$

where dn/dL_{H_α} is the H_α luminosity function (LF)⁷. The mean intensity of the H_α emission is then computed as

$$\bar{I}_{H_\alpha}(z) = \frac{1}{4\pi} \frac{1}{\nu_{H_\alpha} H(z)} \bar{\rho}_{L,H_\alpha}(z), \quad (13)$$

⁷ Note that one can express $\bar{\rho}_{L,H_\alpha}(z)$ by integrating the halo mass function and the SFR-to-halo-mass relation as well. Nevertheless, we think Eq. (12) would give a more reasonable estimate, because the SFR-to-halo-mass relation is poorly constrained at present.

where ν_{H_α} is the rest-frame frequency of the H_α line. Ref. [19] provides a phenomenological model of Eq. (13) using Eq. (12) and the current constraint of LFs at different redshifts. Their model is expressed as

$$\bar{I}_{H_\alpha}(z) = 3.326 \times 10^{-9} \frac{0.027 + 0.28z}{1 + (z/4.8)^{5.3}} 10^{-A_{H_\alpha}/2.5} \times \left(\frac{\nu_{H_\alpha}^{-1} H^{-1}(z)}{h^{-1} \text{ Mpc Hz}^{-1}} \right) \text{ erg/s/cm}^2/\text{Hz/str}. \quad (14)$$

Finally, we express the observed H_α intensity as

$$I_{H_\alpha}(\boldsymbol{\theta} | \nu) = \int d\chi W_{H_\alpha}(z|\nu) [1 + \delta_{H_\alpha}(\mathbf{r}, z)], \quad (15)$$

$$W_{H_\alpha}(z|\nu) = \bar{I}_{H_\alpha}(z) \delta_D^{(1)}(\chi - \chi_{H_\alpha}), \quad (16)$$

where χ_{H_α} is the comoving distance to the redshift z_{H_α} which is defined by $z_{H_\alpha} \equiv \nu_{H_\alpha}/\nu - 1$, and δ_{H_α} is the density contrast in the H_α luminosity density.

In actual observations, several lines can contaminate the observed H_α intensity maps because the measurement relies on spectroscopy at single wavelengths. The contamination lines include ionized oxygen [O_{II}] 372.7 nm and [O_{III}] 500.7 nm lines, the hydrogen H_β 486.1 nm, and Lyman α ($Ly\alpha$) 121.6 nm lines⁸. To take into account these interlopers, we assume the published relations between line luminosity and the SFR. For a given line denoted as Q , we express the luminosity-SFR relation as

$$L_Q^{\text{obs}} = \mathcal{L}_Q \left(\frac{\text{SFR}}{1 M_\odot/\text{yr}} \right), \quad (17)$$

where L_Q^{obs} is the observed luminosity for the line Q , and \mathcal{L}_Q is the scale luminosity in units of erg/s. Note that the term \mathcal{L}_Q includes the dust attenuation effect as $10^{-A_Q/2.5}$ where A_Q is the extinction for the line Q . Using Eqs. (8), (9), (12) and (17), one can find

$$\bar{\rho}_{L,Q} = \frac{\mathcal{L}_Q}{\mathcal{L}_{H_\alpha}} \bar{\rho}_{L,H_\alpha}, \quad (18)$$

where $\bar{\rho}_{L,Q}$ is the luminosity density for the line Q . Table I summarizes the model of \mathcal{L}_Q in this paper.

Hence, the total intensity from astrophysical sources is written as

$$I_{\text{astro}}(\boldsymbol{\theta} | \nu) = \sum_Q \int d\chi W_Q(z|\nu) [1 + \delta_{\text{astro}}(\mathbf{r}, z)], \quad (19)$$

$$W_Q(z|\nu) = \frac{1}{4\pi} \frac{\bar{\rho}_Q}{\nu_Q H(z)} \delta_D^{(1)}(\chi - \chi_Q) = \frac{\mathcal{L}_Q}{\mathcal{L}_{H_\alpha}} \frac{\nu_{H_\alpha}}{\nu_Q} \bar{I}_{H_\alpha}(z) \delta_D^{(1)}(\chi - \chi_Q) \quad (20)$$

⁸ In principle, [N_{II}] 658.3 nm/654.8 nm and [S_{II}] 671.7 nm/673.1 nm doublet lines also contribute to the H_α intensity maps. Nevertheless, the SPHEREx is not able to distinguish the H_α line between these doublet lines in frequency spaces. In this paper, we include the contribution from these doublet lines as follows in Ref. [19]. We assume that the N_{II} line contributes 22% of the sum the H_α and N_{II} line intensities [20], while the S_{II} doublet line intensity is set to 12% of the $H_\alpha + N_{II} + S_{II}$ line intensity [21].

Line	λ_Q (nm)	\mathcal{L}_Q (erg/s)	A_Q (mag)
H α	656.28	$1.26 \times 10^{41} \times 10^{-A_{H\alpha}/2.5}$ (a)	1 (b)
O $_{\text{III}}$	500.7	$1.32 \times 10^{41} \times 10^{-A_{O_{\text{III}}}/2.5}$ (c)	1.35 (d)
H β	486.1	$4.43 \times 10^{40} \times 10^{-A_{H\beta}/2.5}$ (e)	1.35 (f)
O $_{\text{II}}$	372.7	$7.18 \times 10^{40} \times 10^{-A_{O_{\text{II}}}/2.5}$ (g)	0.62 (h)
Ly α	121.6	$1.10 \times 10^{42} \times 10^{-A_{\text{Ly}\alpha}/2.5}$ (i)	0

TABLE I. Characteristics of astrophysical lines in this paper. For a given line Q , λ_Q represents the rest-frame wavelength, \mathcal{L}_Q is the scale luminosity in the luminosity-SFR relation in Eq. (17), and A_Q is the extinction.

^a Ref. [17].

^b Ref. [18].

^c Ref. [22].

^d Ref. [23].

^e Using Eq. (8) and the recombination emission line ratios.

^f Refs. [24, 25].

^g Using a ratio of 0.57 between the O $_{\text{II}}$ and H α fluxes observed in local galaxies [17].

^h Ref. [26].

ⁱ Ref. [17].

where $Q = \{\text{H}\alpha, [\text{O}_{\text{II}}], [\text{O}_{\text{III}}], \text{H}\beta, \text{Ly}\alpha\}$, ν_Q is the rest-frame frequency for the line Q , χ_Q is the comoving distance to the redshift z_Q which is defined by $z_Q \equiv \nu_Q/\nu - 1$, δ_{astro} is the density contrast in the luminosity density of astrophysical sources. Because the luminosity density is always expressed as in Eq. (11) within our framework, statistics of δ_{astro} are determined by the SFR alone, not depending on kinds of lines. To be specific, the field δ_{astro} is given by

$$1 + \delta_{\text{astro}}(\mathbf{r}, z) = \mathcal{N}_{\text{astro}}^{-1}(z) \sum_i \dot{M}_*(M_i, z) \times \delta_{\text{D}}^{(3)}(\mathbf{r} - \mathbf{r}_i) \quad (21)$$

$$\mathcal{N}_{\text{astro}}(z) = \int dM \frac{dn}{dM} \dot{M}_*(M_i, z), \quad (22)$$

where dn/dM is the halo mass function.

B. Weak Lensing

1. Cosmic shear

Weak gravitational lensing effect is usually characterized by the distortion of image of a source object by the following 2D matrix:

$$A_{ij} = \frac{\partial \beta^i}{\partial \theta^j} \equiv \begin{pmatrix} 1 - \kappa - \gamma_1 & -\gamma_2 \\ -\gamma_2 & 1 - \kappa + \gamma_1 \end{pmatrix}, \quad (23)$$

where $\boldsymbol{\theta}$ represents the observed position of a source object, $\boldsymbol{\beta}$ is the true position, κ is the convergence, and γ is the shear. In the weak lensing regime (i.e., $\kappa, \gamma \ll 1$), each component of A_{ij} can be related to the second derivative of the gravitational potential Φ [14]. Using the Poisson equation and the Born approximation, one

can express the weak lensing convergence field as the weighted integral of matter overdensity field $\delta_{\text{m}}(\mathbf{x})$:

$$\kappa(\boldsymbol{\theta}) = \int_0^{\chi_H} d\chi W_{\kappa}(\chi) \delta_{\text{m}}(\mathbf{r}, z), \quad (24)$$

where δ_{m} is the matter overdensity field, χ_H is the comoving distance up to $z \rightarrow \infty$ and $W_{\kappa}(\chi)$ is called lensing kernel. For a given redshift distribution of source galaxies, the lensing kernel is expressed as

$$W_{\kappa}(\chi) = \frac{3}{2} \Omega_{\text{m}0} H_0^2 (1 + z(\chi)) \int_{\chi}^{\chi_H} d\chi' p(\chi') \frac{\chi(\chi' - \chi)}{\chi'}, \quad (25)$$

where $p(\chi)$ represents the redshift distribution of source galaxies normalized to $\int_0^{\chi_H} d\chi p(\chi) = 1$. In this paper, we assume that $p(\chi)$ is expressed as

$$p(\chi) \propto \left(\frac{d\chi}{dz} \right)^{-1} z^{\alpha} \exp \left[- \left(\frac{z}{z_0} \right)^{\beta} \right], \quad (26)$$

where we adopt $\alpha = 1.27$, $\beta = 1.02$, and $z_0 = 0.50$. These parameters are expected in a realistic situation in the LSST [27]. Note that the median source redshift in this model is given by 0.83.

2. Intrinsic alignments of galaxies

Galaxies are thought to be formed at high density regions in the universe, or gravitationally-bound dark matter halos. Such dark matter halos are grown by anisotropic mass accretion through cosmic filaments. Because filamentary structures can introduce tidal interaction of dark matter halos and surrounding density fields, orientation of halo shapes can not be randomly distributed, but aligned with the filaments [28, 29].

Possible large-scale alignments of galaxies' shape even in the absence of gravitational lensing, referred to as intrinsic alignments (IAs), can introduce a systematic uncertainty in any cross correlation analyses based on weak lensing [30]. To account for the IA effect on the cross correlation between line intensity and weak lensing maps, we work with the linear alignment model [31, 32]. In this paper, we set a relevant IA field to lensing convergence so that it can reproduce the E-mode power spectrum of shapes in the linear alignment model [33]. The IA field κ_{IA} is then given by

$$\kappa_{\text{IA}}(\boldsymbol{\theta}) = \int d\chi W_{\text{IA}}(\chi) \delta_{\text{m}}(\mathbf{r}, z), \quad (27)$$

$$W_{\text{IA}}(\chi) = -\mathcal{A}_{\text{IA}} C_1 \frac{\Omega_{\text{m}0} \rho_{\text{crit},0}}{D(z)} \left(\frac{1+z}{1+z_0} \right)^{\eta_{\text{IA}}} p(\chi), \quad (28)$$

where \mathcal{A}_{IA} controls the IA amplitude, η_{IA} is a free parameter to characterize redshift evolution, $C_1 = 5 \times 10^{-14} h^{-2} M_{\odot} \text{Mpc}^3$ is a normalization constant, $z_0 = 0.62$ is the pivot redshift, and $D(z)$ is the normalized linear growth factor, so that $D(0) = 1$. We adopt an

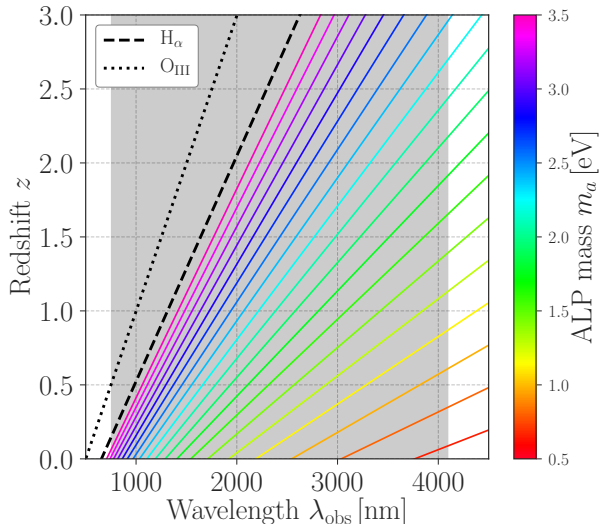


FIG. 1. The relation between observable wavelengths and line redshifts in the SPHEREx. The gray filled region shows the range of wavelengths in the SPHEREx, while the dashed and dotted lines represent the wavelength-redshift relation for H_α and O_{III} lines, respectively. The colored solid lines show the relation for ALP decay lines with various ALP masses m_a . ALPs with smaller m_a emit photons with a longer wavelength as shown in redder lines in this figure.

estimate of $\eta_{IA} = 3$ based on observations of SuperCOSMOS Sky Survey [34] and Subaru Hyper Suprime Cam [35], while we set $\mathcal{A}_{IA} = 1$ for our fiducial model. Note that some recent weak-lensing measurements reported a marginal non-zero \mathcal{A}_{IA} [35–37], but the exact value should depend on the selection of source galaxies used in weak lensing analyses.

C. Relevant redshift ranges

We here describe effective redshift ranges to the cross correlation analysis between line intensity and weak lensing maps. For the line intensity maps, we consider the SPHEREx survey observing an all sky in optical and near-infrared wavelengths. The SPHEREx will provide line intensity maps at wavelengths of 750–4100 nm with a frequency resolution being $R = 41.5$ [38].

Figure 1 shows the relation between observed wavelengths λ_{obs} and line redshifts in the SPHEREx. Different colored solid lines represent line redshifts by ALP decays with a variety of ALP masses m_a . For the wavelength range in the SPHEREx, we expect that ALP decays with $0.5 \lesssim m_a [\text{eV}] \lesssim 3.5$ would be relevant to the cross correlation. For $m_a \gtrsim 3.5 \text{ eV}$, the wavelength by ALP-decay line becomes shorter than those of astrophysical lines such as H_α and O_{III} . Because the weak lensing can probe large-scale structures at $z \sim 0.5$ in modern galaxy surveys, the ALP decay with $m_a \gtrsim 3.5 \text{ eV}$ is not expected to induce a significant correlation between the

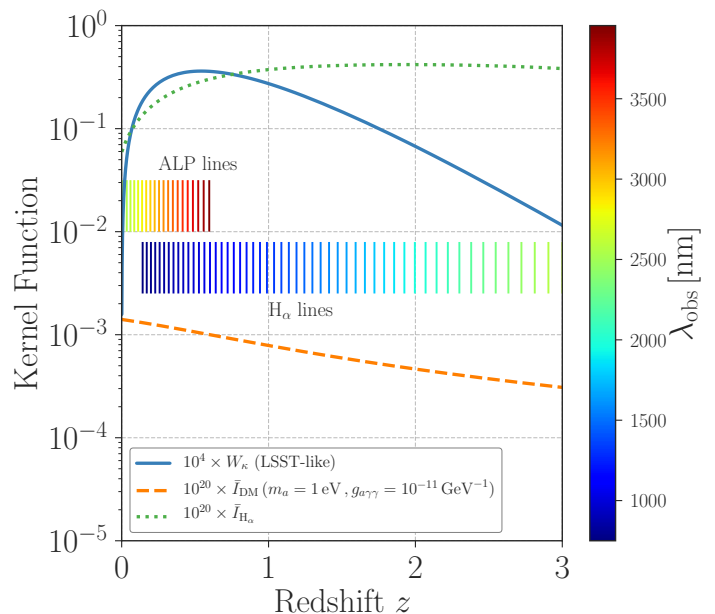


FIG. 2. Relevant redshift ranges in the line intensity and weak lensing maps. In this figure, we assume an LSST-like imaging survey for the lensing map. The blue solid line shows the lensing kernel function W_κ for the LSST-like survey, while the green dotted line represents our fiducial model of the mean intensity for H_α line. The orange dashed line is the mean intensity as a function of redshift z for ALPs with a mass of $m_a = 1 \text{ eV}$ and a particle-to-photons coupling of $g_{a\gamma\gamma} = 1 \times 10^{-11} \text{ GeV}^{-1}$. Note that the mean intensity is defined in units of $\text{erg/s/cm}^2/\text{Hz/str}$. Different line segments at the middle in this figure represent relevant redshifts to line-intensity measurements for given observed wavelengths λ_{obs} . The right color bar covers the range of λ_{obs} in SPHEREx. For instance, when using a line intensity map at $\lambda_{\text{obs}} \sim 2500 \text{ nm}$, one will probe large-scale structures at $z \sim 0.1$ by the ALP decay, while the H_α line provides astrophysical information at $z \sim 3$. Because the lensing is efficient to extract the information about structures at $z \sim 0.3$, the cross correlation with the line intensity and weak lensing maps allows us to separate ALP-decay signals from the total line intensity when λ_{obs} is limited to be greater than $\sim 2500 \text{ nm}$.

lensing and the SPHEREx intensity maps. On the other hand, the wavelength coverage in the SPHEREx does not allow us to detect the line emission from the ALP decay with $m_a \lesssim 0.5 \text{ eV}$.

Figure 2 summarizes the relevant redshift range to the cross correlation with line-intensity and weak-lensing maps. In this figure, the blue solid line represents the lensing kernel defined in Eq. (25) for the expected source-redshift distribution in the LSST. The LSST can be the most efficient to probe the large-scale cosmic mass density at $z \simeq 0.3 - 0.6$. For comparison, the orange dashed line shows the function of

$$\bar{I}_{\text{DM}}(z) = \frac{\Gamma}{4\pi} \frac{\Omega_{\text{DM}} \rho_{\text{crit},0}}{\nu_a H(z)}, \quad (29)$$

where this provides the redshift dependence on the mean

line intensity by the ALP decay. In Figure 2, we consider a representative example as ALPs with $m_a = 1$ eV and $g_{a\gamma\gamma} = 1 \times 10^{-11} \text{ GeV}^{-1}$. In addition, the green dotted line shows the mean H_α line intensity defined in Eq. (13). For the line intensity mapping, we measure the cumulative emission from any photon sources at a given wavelength λ_{obs} . The line segments at the middle of Figure 2 highlight effective redshifts in the line-intensity map as a function of λ_{obs} . According to the relation between line redshifts and λ_{obs} in Figure 1, the ALP-decay line can *always* provide lower-redshift information than the H_α line as long as we limit the particle mass to be $m_a \lesssim 3.5$ eV. Because the lensing measurement mainly carries the information at $z \lesssim 1$ in the LSST, the cross correlation between the SPHEREx line intensity and the LSST weak lensing allows us to extract the ALP-decay signal alone in an efficient way when one measures the correlation as a function of λ_{obs} .

III. STATISTICS

We here define the statistic of interest, i.e. the cross correlation between the line intensity and weak lensing maps.

A. Cross Correlation Functions

For a given set of two different random fields $X(\boldsymbol{\theta})$ and $Y(\boldsymbol{\theta})$, the cross correlation function is defined as

$$\xi_{XY}(\boldsymbol{\theta}) = \langle X(\boldsymbol{\phi})Y(\boldsymbol{\phi} + \boldsymbol{\theta}) \rangle, \quad (30)$$

where $\langle \dots \rangle$ represents an ensemble average. The Fourier transform of Eq. (30) is known as the cross power spectrum and it is given by

$$\langle \tilde{X}(\boldsymbol{\ell})\tilde{Y}(\boldsymbol{\ell}') \rangle = (2\pi)^2 C_{XY}(\boldsymbol{\ell}) \delta_{\text{D}}^{(2)}(\boldsymbol{\ell} - \boldsymbol{\ell}'), \quad (31)$$

where C_{XY} is the cross power spectrum, \tilde{X} represents the Fourier transform of the field X , and so on. In this paper, we use the cross power spectrum to study the cross correlation between the line intensity and weak lensing maps.

As shown in Section II, the observed maps are decomposed into

$$I_{\text{obs}}(\boldsymbol{\theta} | \nu) = I_a(\boldsymbol{\theta} | \nu) + I_{\text{astro}}(\boldsymbol{\theta} | \nu) + I_{\text{N}}(\boldsymbol{\theta} | \nu), \quad (32)$$

$$\kappa_{\text{obs}}(\boldsymbol{\theta}) = \kappa(\boldsymbol{\theta}) + \kappa_{\text{IA}}(\boldsymbol{\theta}) + \kappa_{\text{N}}(\boldsymbol{\theta}), \quad (33)$$

where we denote I_{obs} and κ_{obs} as the observed line intensity and weak lensing maps, respectively. Apart from the components as described in Section II, we include observational noise terms in Eqs. (32) and (33). The noise in the line intensity map I_{N} will be dominated by photo noise from zodiacal light in the SPHEREx [38], which is diffuse and nearly uniform across the field of view. On the other hand, the noise in the weak lensing map κ_{N} mainly arises from the intrinsic scatter in galaxy shapes.

Hence, the cross power spectrum between I_{obs} and κ_{obs} has four different contributions as

$$C_{\text{LIM}-\kappa}^{(\text{obs})}(\boldsymbol{\ell} | \nu) = C_{\text{ALP}-\kappa}(\boldsymbol{\ell} | \nu) + C_{\text{ALP-IA}}(\boldsymbol{\ell} | \nu) + C_{\text{astro}-\kappa}(\boldsymbol{\ell} | \nu) + C_{\text{astro-IA}}(\boldsymbol{\ell} | \nu), \quad (34)$$

where $C_{\text{ALP}-\kappa}$ is the cross correlation between the ALP-decay line and cosmic shear, $C_{\text{ALP-IA}}$ is the cross correlation between the ALP-decay line and IA terms, $C_{\text{astro}-\kappa}$ is the cross correlation between the astrophysical lines and cosmic shear, and $C_{\text{astro-IA}}$ is the cross correlation between the astrophysical lines and IA terms. Note that the noise terms I_{N} and κ_{N} are assumed to be uncorrelated with other fields. In the following, we evaluate each term in the right hand side of Eq. (34).

B. Model

1. ALP decay line and cosmic shear

The term $C_{\text{ALP}-\kappa}$ represents the cross correlation between the ALP decay line and cosmic shear. Note that the ALP decay line exactly traces the dark matter distribution in the universe (see Eq. [5]), while cosmic shear, or lensing convergence κ provides an unbiased estimate of projected total mass density with some weight function along a line of sight (see Eq. [24]). Using the Limber approximation [39], we can express the cross power spectrum as

$$C_{\text{ALP}-\kappa}(\boldsymbol{\ell} | \nu) = \int d\chi \frac{W_{\text{DM}}(z|\nu) W_{\kappa}(z)}{\chi^2} P_{\text{DM}-m} \left(\frac{\ell}{\chi}, z(\chi) \right) = \frac{\bar{I}_{\text{DM}}(\chi_a) W_{\kappa}(\chi_a)}{\chi_a^2} P_{\text{DM}-m} \left(\frac{\ell}{\chi_a}, z_a \right), \quad (35)$$

where $P_{\text{DM}-m}(k, z)$ is the three-dimensional cross power spectrum between the dark matter and total mass density fields. Throughout this paper, we assume that the dark-matter overdensity field is expressed as $(\Omega_{\text{DM}}/\Omega_{\text{m0}}) \delta_{\text{m}}$. Then, the cross power spectrum is given by

$$P_{\text{DM}-m}(k, z) = \frac{\Omega_{\text{DM}}}{\Omega_{\text{m0}}} P_{\text{m}}(k, z), \quad (36)$$

where $P_{\text{m}}(k, z)$ is the three-dimensional non-linear matter power spectrum. In the following, we adopt a simulation-calibrated fitting formula [40] to compute $P_{\text{m}}(k, z)$. It would be worth noting that we ignore possible baryonic effects on $P_{\text{DM}-m}(k, z)$, while it may induce a $\lesssim 30\%$ level systematic error in our forecasts on the constraint of Γ (see Ref. [41] for a review of baryonic effects on large-scale structures). Since the decay rate Γ is proportional to $g_{a\gamma\gamma}^2$, we expect that the constraint of $g_{a\gamma\gamma}$ can be affected by the baryonic effects with a level of $\lesssim 15\%$ at most. One needs to account for this systematic error in real measurements, but it does not play a central role in our forecasts.

2. ALP decay line and intrinsic alignments

Similarly, the cross correlation between the ALP decay line and IA terms is given by

$$C_{\text{ALP-IA}}(\ell|\nu) = \frac{\bar{I}_{\text{DM}}(\chi_a) W_{\text{IA}}(\chi_a)}{\chi_a^2} \times P_{\text{DM-m}}\left(\frac{\ell}{\chi_a}, z_a\right), \quad (37)$$

where this term is strongly degenerate with $C_{\text{ALP-}\kappa}(\ell|\nu)$ at a given ν , because either is proportional to $P_{\text{DM-m}}$ at the same redshift of z_a . Nevertheless, one can constrain an unknown IA parameter \mathcal{A}_{IA} in the function of W_{IA} and break the degeneracy when using the frequency-dependence on $C_{\text{ALP-IA}}(\ell|\nu)$. The frequency dependence on $C_{\text{ALP-IA}}(\ell|\nu)$ can not be same as that of $C_{\text{ALP-}\kappa}(\ell|\nu)$, because the kernel functions W_{κ} and W_{IA} exhibit the different redshift-dependence.

3. Astrophysical lines and cosmic shear

Under the Limber approximation with Eqs. (19) and (24), we can write the term $C_{\text{astro-}\kappa}$ as

$$C_{\text{astro-}\kappa}(\ell|\nu) = \sum_Q \frac{\mathcal{L}_Q \nu_{\text{H}\alpha}}{\mathcal{L}_{\text{H}\alpha} \nu_Q} \frac{\bar{I}_{\text{H}\alpha}(z_Q) W_{\kappa}(z_Q)}{\chi_Q^2} \times P_{\text{astro-m}}\left(\frac{\ell}{\chi_Q}, z_Q\right), \quad (38)$$

where $P_{\text{astro-m}}(k, z)$ is the three-dimensional power spectrum between two fields of δ_{astro} and δ_{m} (see Eq. [21] for our definition of δ_{astro}).

In this paper, we compute $P_{\text{astro-m}}(k, z)$ based on a halo-model approach [42]. Within the halo model, the power spectrum can be decomposed into two terms. One is the one-halo term arising from two-point correlations in single dark matter halos, and another is the two-halo term given by two-point correlations between neighboring halos. Each term can be expressed as

$$P_{\text{astro-m}}(k, z) = P_{\text{astro-m}}^{\text{1h}}(k, z) + P_{\text{astro-m}}^{\text{2h}}(k, z), \quad (39)$$

where $P_{\text{astro-m}}^{\text{1h}}$ and $P_{\text{astro-m}}^{\text{2h}}$ are the one-halo and the two-halo terms, respectively, and

$$P_{\text{astro-m}}^{\text{1h}}(k, z) = \mathcal{N}_{\text{astro}}^{-1}(z) \int dM \frac{dn}{dM} \frac{\rho_h(k|M, z)}{\bar{\rho}_m} \times \dot{M}_*(M, z), \quad (40)$$

$$P_{\text{astro-m}}^{\text{2h}}(k, z) = \left(\int dM \frac{dn}{dM} b_h(M, z) \frac{\rho_h(k|M, z)}{\bar{\rho}_m} \right) \times \left(\mathcal{N}_{\text{astro}}^{-1}(z) \int dM \frac{dn}{dM} b_h(M, z) \dot{M}_*(M, z) \right) \times P_L(k, z), \quad (41)$$

where $\rho_h(k|M, z)$ is the Fourier transform of a spherical halo density profile, $\bar{\rho}_m = \rho_{\text{crit},0} \Omega_{\text{m}0}$, b_h is the linear halo

bias and P_L is the linear matter power spectrum. In the halo-model computations, we define the halo mass as the mass of a spherical overdensity with 200-times the mean density of the universe. For the halo density profile, we adopt the analytical Navarro-Frenk-White (NFW) profile [43], where we use the concentration-mass-redshift relation in Ref. [44]. We also use the fitting formulas of the halo mass function [45] and the linear halo bias [46]. The key ingredient in the computation of Eq. (39) is the SFR as a function of halo masses and redshifts, $\dot{M}_*(M, z)$. Although this quantity is still uncertain, we adopt a simulation-based fitting formula as in Ref. [19] for our baseline model. Their model of $\dot{M}_*(M, z)$ has a form of

$$\dot{M}_*(M, z) = 10^{a(z)} \left(\frac{M}{M_1}\right)^{b(z)} \left(1 + \frac{M}{M_2(z)}\right)^{c(z)}, \quad (42)$$

where $M_1 = 10^8 M_{\odot}$ and there exist four parameters of $a(z), b(z), c(z)$ and $M_2(z)$ in the model. Ref. [19] have provided the parameters at $z = 0, 0.8, 1, 2.2$ and 4.8 by analyzing semi-analytic galaxy catalogs in Ref. [47]. We infer $a(z), b(z), c(z)$ and $M_2(z)$ at a given z by employing a linear interpolation of the fitting results at $z = 0, 0.8, 1, 2.2$ and 4.8 . Note that $b \sim 2.6$, $c \sim -3$ and M_2 ranges from $10^{11-12} M_{\odot}$ over redshifts. Hence, a typical halo mass in the SFR activity (i.e. the mass of the halo which most efficiently produces stars) is set to be $M \sim 10^{12-13} M_{\odot}$ in this model. Although our baseline model would provide an order-of-magnitude estimate for $P_{\text{astro-m}}$, it is based on the semi-analytic model of galaxy formation and poorly constrained by observations. To account for theoretical uncertainties in our model, we introduce two dimensionless parameters $\mathcal{A}_{\text{astro}}$ and η_{astro} , which control the overall amplitude and redshift evolution in $P_{\text{astro-m}}$. To be specific, we set

$$P_{\text{astro-m}}(k, z) \rightarrow \mathcal{A}_{\text{astro}}(1+z)^{\eta_{\text{astro}}} P_{\text{astro-m}}(k, z) \quad (43)$$

when computing $C_{\text{astro-}\kappa}(\ell|\nu)$. For our fiducial model, we adopt $\mathcal{A}_{\text{astro}} = 1$ and $\eta_{\text{astro}} = 0$.

4. Astrophysical lines and intrinsic alignments

The cross correlation between the astrophysical lines and the IA field is then expressed as

$$C_{\text{astro-IA}}(\ell|\nu) = \sum_Q \frac{\mathcal{L}_Q \nu_{\text{H}\alpha}}{\mathcal{L}_{\text{H}\alpha} \nu_Q} \frac{\bar{I}_{\text{H}\alpha}(z_Q) W_{\text{IA}}(z_Q)}{\chi_Q^2} \times \mathcal{A}_{\text{astro}}(1+z_Q)^{\eta_{\text{astro}}} \times P_{\text{astro-m}}\left(\frac{\ell}{\chi_Q}, z_Q\right). \quad (44)$$

C. Survey specifications and statistical errors

We here describe observational parameters of line intensity and weak lensing surveys in our analysis and sum-

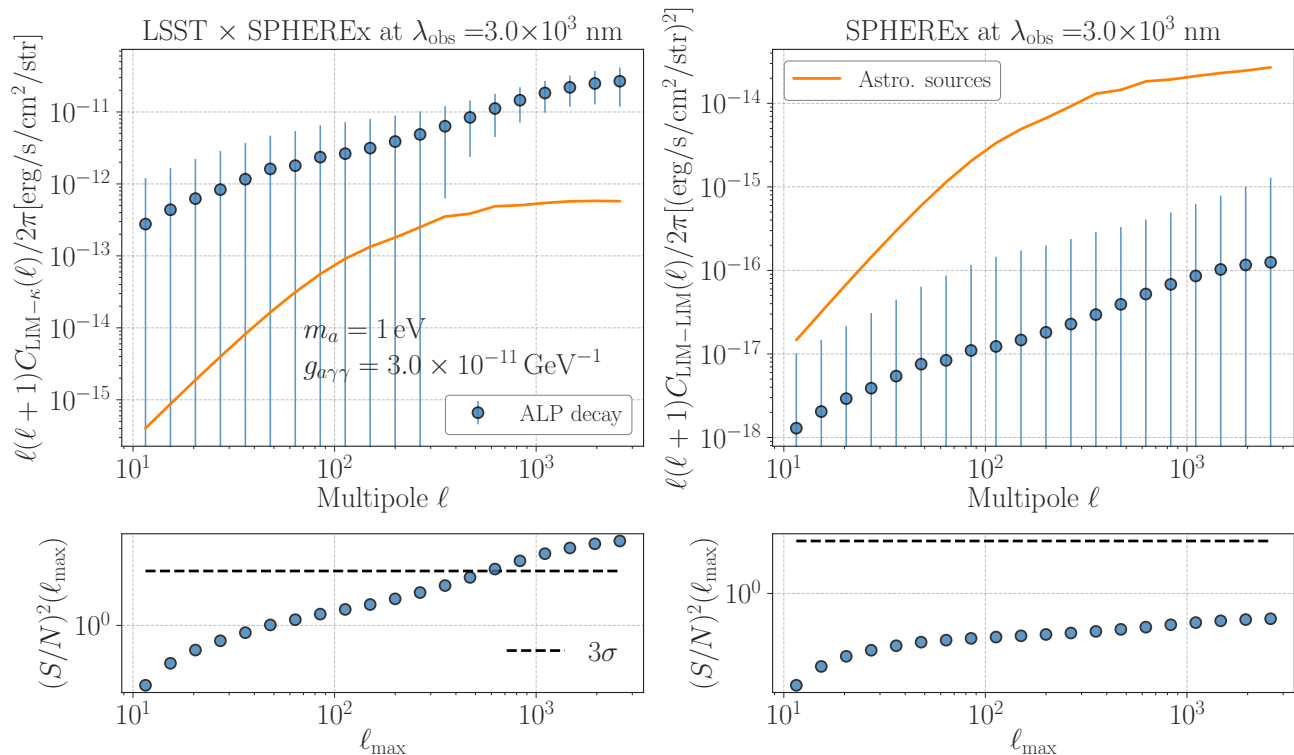


FIG. 3. Expected signals of the cross-correlation function with the line intensity and weak lensing maps as well as the auto correlation of the line intensity map. In this figure, we assume an LSST-like imaging survey for lensing and an SPHEREx-like spectroscopic survey at wavelength $\lambda_{\text{obs}} = 3000$ nm. Details of the survey specification are found in Section III C. The left panels show the cross power spectra and its cumulative signal-to-noise ratio. In the left top, blue points with error bars show the ALP-decay signal for an ALP mass of $m_a = 1$ eV and a particle-to-photons coupling of $g_{a\gamma\gamma} = 3 \times 10^{-11} \text{ GeV}^{-1}$. For comparison, the orange line shows our fiducial model of astrophysical contributions to the cross power spectrum. The left bottom panel represents the cumulative signal-to-noise ratio of the ALP-decay signal as a function of the maximum multipole ℓ_{max} . The black dashed line in the bottom indicates a 3σ -level detection. The right panels are similar to the left, but those are for the auto power spectrum of the intensity map. This figure highlights that the cross power spectrum with the line intensity and weak lensing maps can be dominated by the ALP-decay signal, while the auto power spectrum of the intensity maps will be largely determined by the astrophysical sources.

marize how to set expected statistical uncertainties of Eq. (34).

For line intensity maps, we assume a hypothetical SPHEREx-like survey covering a full sky. Among several observational modes in SPHEREx, we consider the all-sky survey mode with an angular resolution of 0.1 arcmin and a 5σ -level point-source sensitivity of 18.5 AB magnitude per pixel [38]. Note that there exists the “deep” survey mode in SPHEREx and it will have a much greater point-source sensitivity. Hence, the deep survey mode would allow us to perform robust line-intensity mapping measurements, while the sky coverage is planned to be 200 deg^2 only. Because the statistical uncertainty in our cross correlation analysis scales with the inverse of the survey area, the deep survey mode is not suitable to search for large-scale cross correlation signals. We also assume the frequency resolution of $R = 41.5$ at wavelengths of 750 – 4100 nm.

For weak lensing maps, we assume a LSST-like imag-

ing survey covering a sky of 18000 deg^2 . In weak lensing measurements, we assume the source number density of 26 arcmin^{-2} , the intrinsic scatter of galaxy ellipticity per components being 0.26, and the source redshift distribution as in Eq. (26). These survey parameters have been investigated in Ref. [27].

Given survey configurations, we can evaluate the statistical uncertainty of Eq. (34) by using covariance matrices. Assuming that the observable fields follow Gaussian, we can write the covariance matrix as

$$\begin{aligned} \mathbf{C}(\ell, \nu | \ell', \nu') &\equiv \text{Cov} \left[C_{\text{LIM}-\kappa}^{(\text{obs})}(\ell | \nu), C_{\text{LIM}-\kappa}^{(\text{obs})}(\ell' | \nu') \right] \\ &= \frac{\delta_{\ell\ell'}^K}{2\ell \Delta\ell f_{\text{sky}}} \left[C_{\text{LIM-LIM}}^{(\text{obs})}(\ell | \nu, \nu') C_{\kappa-\kappa}^{(\text{obs})}(\ell) \right. \\ &\quad \left. + C_{\text{LIM}-\kappa}^{(\text{obs})}(\ell | \nu) C_{\text{LIM}-\kappa}^{(\text{obs})}(\ell' | \nu') \right], \end{aligned} \quad (45)$$

where f_{sky} is the fraction of sky coverage used in the cross correlation analysis, δ_{ij}^K is the Kronecker delta symbol, $C_{\text{LIM-LIM}}^{(\text{obs})}(\ell | \nu, \nu')$ represents the cross power spec-

trum between two intensity maps with different frequency bands, and $C_{\kappa-\kappa}^{(\text{obs})}(\ell)$ is the auto power spectrum of the observed convergence field (Eq. [33]). The derivation of Eq. (45) is found in Appendix A. Note that f_{sky} is set to be $18,000/41,252.96 = 0.436$ for our case. In Eq. (45), we employ a binning in the multipole ℓ for the measurements of cross power spectra with the bin width being $\Delta\ell$. In this setup, the covariance matrix becomes non-zero only when two different ℓ bins have an identical value. We summarize our model of $C_{\text{LIM-LIM}}^{(\text{obs})}(\ell|\nu, \nu')$ and $C_{\kappa-\kappa}^{(\text{obs})}(\ell)$ in Appendix A.

IV. RESULTS

In this section, we show our main results in this paper. When computing power spectra, we employ a logarithmic binning in the range of $10 < \ell < 3000$ with the number of bins being 20. Also, we compute all power spectra with respect to $\nu I(\theta|\nu)$ in units of $\text{erg/s/cm}^2/\text{str}$.

A. Expected Signal

Let us first consider expected signals in the cross correlation analysis. As a representative example, we assume ALPs with a mass of $m_a = 1 \text{ eV}$ and a particle-to-photons coupling of $g_{a\gamma\gamma} = 3 \times 10^{-11} \text{ GeV}^{-1}$. The top left panel in Fig. 3 shows our baseline model for the cross power spectrum between line intensity maps and weak lensing convergence. In the figure, we suppose the line intensity map at $\lambda_{\text{obs}} = 3000 \text{ nm}$. The blue points with error bars represent the ALP-decay signal $C_{\text{ALP}-\kappa}$, while the orange line stands for the astrophysical contribution $C_{\text{astro}-\kappa}$. In the left bottom, we characterize the detectability of the signal $C_{\text{ALP}-\kappa}$ by introducing the cumulative signal-to-noise ratio. The signal-to-noise ratio at a given photon frequency is defined as

$$(S/N)^2(\ell_{\text{max}}) = \sum_{\ell_i, \ell_j \leq \ell_{\text{max}}} C_{\text{ALP}-\kappa}(\ell_i|\nu) C_{\text{null}}^{-1}(\ell_i, \nu|\ell_j, \nu) \times C_{\text{ALP}-\kappa}(\ell_j|\nu), \quad (46)$$

where C_{null} is the covariance matrix when we set the decay rate to be $\Gamma = 0$. Hence, Eq. (46) can be used to compute the significance of the ALP-decay signal over a null detection hypothesis. The blue points in the left bottom panel in Fig. 3 shows the signal-to-noise ratio as a function of maximum multipoles ℓ_{max} in the analysis, while the dashed line represents a 3σ -level significance.

On the other hand, the right panels in Fig. 3 summarize the results for the auto power spectrum in the intensity map. We compute the expected auto correlation signal as in Appendix A. In the top right panel, the orange line shows the auto power spectrum arising from clustering of astrophysical lines (referred to as $C_{\text{astro-astro}}$ in Appendix A). The blue points with error bars are the counterpart of the ALP decay line, $C_{\text{ALP-ALP}}$ as defined

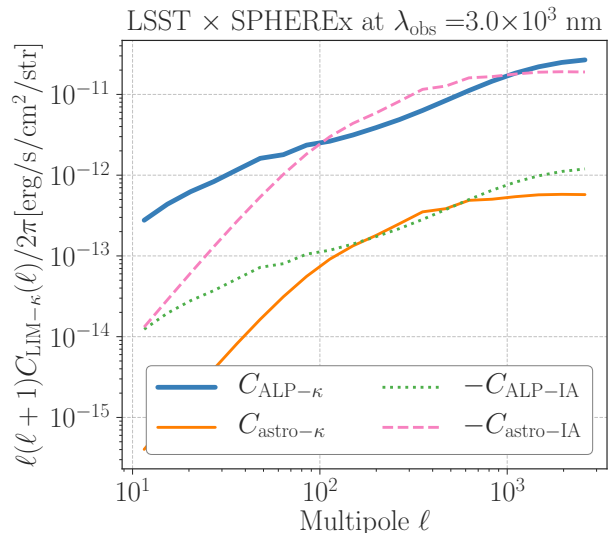


FIG. 4. Separated contributions to the observed cross power spectrum between line intensity and weak lensing maps. We here suppose the LSST-like source galaxy distribution for lensing and the line intensity map at $\lambda_{\text{obs}} = 3000 \text{ nm}$. For the ALP decay, we consider the ALPs with a mass of $m_a = 1 \text{ eV}$ and a particle-to-photons coupling of $g_{a\gamma\gamma} = 3 \times 10^{-11} \text{ GeV}^{-1}$. The blue thick line shows the cross correlation between the ALP decay line and weak lensing convergence, while the orange thin line stands for the counterpart of astrophysical lines. The green dotted and pink dashed lines represent the IA-induced signals arising from the ALP decay and astrophysical lines, respectively. Note that the IA-induced signal becomes negative over the angular scales of interest.

in Eq. (A10). The error bars in the top right panel are computed as

$$\text{Cov} \left[C_{\text{LIM-LIM}}^{(\text{obs})}(\ell|\nu), C_{\text{LIM-LIM}}^{(\text{obs})}(\ell'|\nu) \right] = \frac{\delta_{\ell\ell'}^K}{\ell \Delta\ell f_{\text{sky}}} C_{\text{LIM-LIM}}^{(\text{obs})}(\ell|\nu) C_{\kappa-\kappa}^{(\text{obs})}(\ell), \quad (47)$$

where details of $C_{\text{LIM-LIM}}^{(\text{obs})}$ and $C_{\kappa-\kappa}^{(\text{obs})}$ are given in Appendix A. The signal-to-noise ratio of $C_{\text{ALP-ALP}}$ can be computed in a similar way to Eq. (46) and it is shown in the bottom right panel in Fig. 3.

The comparisons between left and right panels in Fig. 3 clarify that the ALP decay can induce a significant correlation signal compared to the counterpart of astrophysical lines in the cross correlation analysis, but not in the auto correlation of line intensity maps. This can be understood as the cross correlation between line intensity and weak lensing maps can probe lower-redshift large-scale structures and the ALP decay line mainly comes from those lower-redshift structures. As shown in Fig. 2, the auto correlation function will be dominated by astrophysical lines and the astrophysical lines effectively probe higher redshifts at $z \gtrsim 2$ as long as the observed wavelength is set to be $\lambda_{\text{obs}} \gtrsim 2000 \text{ nm}$.

Apart from gravitational lensing effects, we will have

the cross correlation arising from the IA effects of galaxy shapes. Fig. 4 summarizes our baseline model of the cross power spectrum between line intensity and weak lensing maps. Different colored lines in the figure show four separated terms in the observed power spectrum as in Eq. (34). Note that the IA-induced terms ($C_{\text{astro-IA}}$ and $C_{\text{ALP-IA}}$) will show a negative value because major axes in galaxy shapes are expected to align in the radial direction toward high density regions [31, 32]. Our baseline model shows that the cross correlation between astrophysical lines and intrinsic galaxy shapes can dominate the ALP-decay-induced lensing signal at $\ell \lesssim 1000$, while the term $C_{\text{ALP-}\kappa}$ still has a significant contribution to the observed signal at small angular scales of $\ell \gtrsim 1000$. We explore the detectability of $C_{\text{ALP-}\kappa}$ in the presence of the IA effects in Section IV C.

B. Signal-to-noise ratios

The lensing kernel function is relatively broad in redshifts and the effective redshift for the ALP decay can vary as we change frequency bands in the intensity map (see Fig. 2). Hence, combining the cross power spectra among multi-frequency bands can further improve the detectability of the ALP decay line. The total signal-to-noise ratio of the ALP-decay signal in the range of observed frequency $\nu_{\min} \leq \nu \leq \nu_{\max}$ can be defined as

$$(S/N)_{\text{tot}}^2(\ell_{\max}|\nu_{\min}, \nu_{\max}) = \sum_{\nu_{\alpha}, \nu_{\beta}} \sum_{\ell_i, \ell_j \leq \ell_{\max}} C_{\text{ALP-}\kappa}(\ell_i|\nu_{\alpha}) \times C_{\text{null}}^{-1}(\ell_i, \nu_{\alpha}|\ell_j, \nu_{\beta}) C_{\text{ALP-}\kappa}(\ell_j|\nu_{\beta}), \quad (48)$$

where we impose $\nu_{\min} \leq \nu_{\alpha}, \nu_{\beta} \leq \nu_{\max}$ to take the sum. In our case, we assume the SPHEREx-like situation with the wavelength coverage of 750–4100 nm, corresponding to $\nu_{\min} = 73.1$ THz and $\nu_{\max} = 399.7$ THz. When setting the frequency resolution being $R = 41.5$, we find that 70 intensity maps are available in total.

For a given m_a , we can express the total signal-to-noise ratio as

$$(S/N)_{\text{tot}}(\ell_{\max}) = \left[\frac{\Gamma}{\Gamma_{\text{upp}}(\ell_{\max})} \right] \quad (49)$$

$$= \left[\frac{g_{a\gamma\gamma}}{g_{a\gamma\gamma, \text{upp}}(\ell_{\max})} \right]^2. \quad (50)$$

Fig. 5 shows Γ_{upp} and $g_{a\gamma\gamma, \text{upp}}$ for ALPs with a particle mass of $m_a = 1$ eV. We find that combining the cross power spectra at multi-frequency bands allows us to probe the particle-to-photon coupling down to $g_{a\gamma\gamma} \sim 1 \times 10^{-11} \text{ GeV}^{-1}$ if we can have a precise model of the cross power spectra at $\ell \lesssim 800$.

Fig. 6 summarizes expected 2σ upper limits of $g_{a\gamma\gamma}$ for different particle masses m_a if the cross correlation analysis in LSST and SPHEREx is consistent with a null detection. Note that we set $\ell_{\max} = 2000$ in Fig. 6. In the figure, we also show several observational constraints in the literature for comparison. Those include the study of

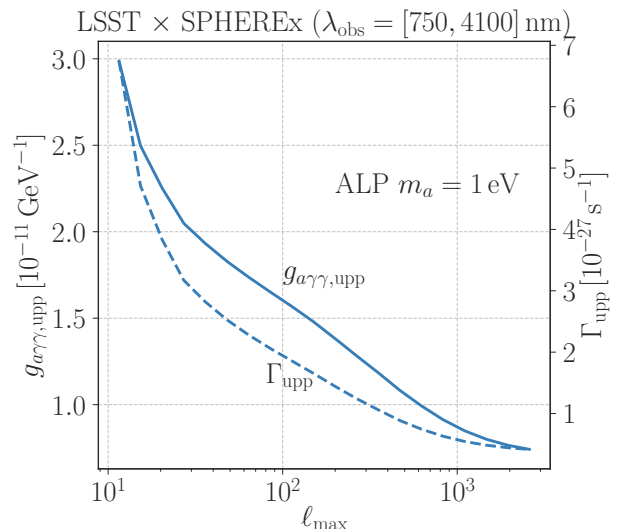


FIG. 5. Total signal-to-noise ratio of the cross power spectrum between the line intensity and weak lensing maps for ALPs with a particle mass of $m_a = 1$ eV. For a fixed mass m_a , the total signal-to-noise ratio is given by $(S/N)_{\text{tot}} = (g_{a\gamma\gamma}/g_{a\gamma\gamma, \text{upp}})^2 = \Gamma/\Gamma_{\text{upp}}$, where $g_{a\gamma\gamma}$ is the particle-to-photon coupling constant for ALPs and Γ is the ALP decay rate. The solid line and dashed lines show $g_{a\gamma\gamma, \text{upp}}$ and Γ_{upp} as a function of the maximum multipole ℓ_{\max} in the cross-correlation analysis, respectively. In this figure, we combine the cross power spectra defined with multiple-wavelength intensity maps in the range of $\lambda_{\text{obs}} = 750 - 4100$ nm. Also, we assume that a sky of $18,000 \text{ deg}^2$ is available for the analysis.

stellar evolution of horizontal branch (HB) to red giants in globular clusters [48], “axion helioscope” observations by the CERN Axion Solar Telescope (CAST) [49], spectroscopic observations of the dwarf spheroidal galaxy Leo T by the Multi Unit Spectroscopic Explorer (MUSE) [50]. The blue filled region in Fig. 6 represents the expected constraint by the LSST-SPHEREx cross correlation analysis, enabling us to improve the existing constraint at $m_a = 1 - 2.7$ eV by a factor of 6–10. For the interested readers, we also provide a forecast in terms of the dark matter lifetime Γ in Appendix B.

C. Forecast of ALP parameter constraints

In actual observations, we have several expected components in the cross correlation between line intensity and weak lensing maps as in Eq. (34). As shown in Fig. 4, the cross correlation caused by the astrophysical lines and the IA effect of galaxy shapes $C_{\text{astro-IA}}$ is expected to prevent us from inferring the ALP parameters from the observed power spectra. To study impacts of $C_{\text{astro-IA}}$ on constraints of the ALP parameters, we perform a Fisher analysis for cross correlation analyses in LSST and SPHEREx. The Fisher matrix is commonly used to assess expected constraints of parameters of in-

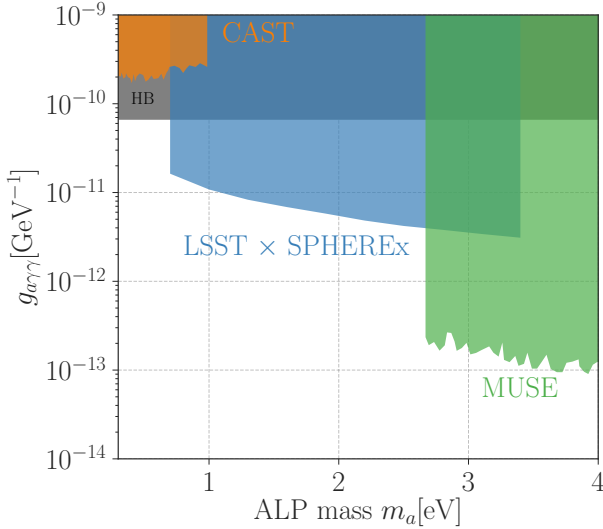


FIG. 6. 2σ -level upper limits of the ALP-to-photons coupling $g_{a\gamma\gamma}$ as a function of ALP mass m_a . The blue region can be excluded by the cross correlation analysis with SPHEREx line intensity maps and LSST lensing. For comparison, we show existing constraints in the literature; the gray, orange, and green regions have been excluded by the study of stellar evolution of horizontal branch (HB) to red giants in globular clusters [48], the CERN Axion Solar Telescope (CAST) [49], spectroscopic observations of the dwarf spheroidal galaxy Leo T by the Multi Unit Spectroscopic Explorer (MUSE) [50], respectively.

terest with given observables. In our case, it is computed as

$$F_{\alpha\beta} = \sum_{i,j,p,q} \frac{\partial C_{\text{LIM}-\kappa}^{(\text{obs})}(\ell_i|\nu_p)}{\partial s_\alpha} \mathbf{C}^{-1}(\ell_i, \nu_p|\ell_j, \nu_q) \times \frac{\partial C_{\text{LIM}-\kappa}^{(\text{obs})}(\ell_j|\nu_q)}{\partial s_\beta}, \quad (51)$$

where $C_{\text{LIM}-\kappa}^{(\text{obs})}(\ell_i|\nu_p)$ represents the observed power spectrum at the i -th ℓ bin for the intensity map with the observed frequency being ν_p , \mathbf{C} is the covariance matrix of $C_{\text{LIM}-\kappa}^{(\text{obs})}$ as in Eq. (45), and s_α is the α -th parameter. The inverse of the Fisher matrix provides an estimate of the error covariance for two parameters as

$$F_{\alpha\beta}^{-1} = \langle \Delta s_\alpha \Delta s_\beta \rangle, \quad (52)$$

where Δs_α is the statistical uncertainty of parameter s_α .

In our Fisher analysis, we consider the following parameters to vary: $\mathbf{s} = \{m_a, g_{a\gamma\gamma}, \mathcal{A}_{\text{IA}}, \eta_{\text{IA}}, \mathcal{A}_{\text{astro}}, \eta_{\text{astro}}\}$. The fiducial values of our parameters is set to $\mathbf{s}_{\text{fid}} = \{1 \text{ eV}, 1 \times 10^{-11} \text{ GeV}^{-1}, 1, 3, 1, 0\}$. When computing the Fisher matrix, we limit the range of multipoles as $10 < \ell \leq \ell_{\text{max}}$ and examine three cases of $\ell_{\text{max}} = 500, 1000,$ and 2000 . Changing ℓ_{max} in our Fisher matrix tells us how smaller-scale information will help to improve the

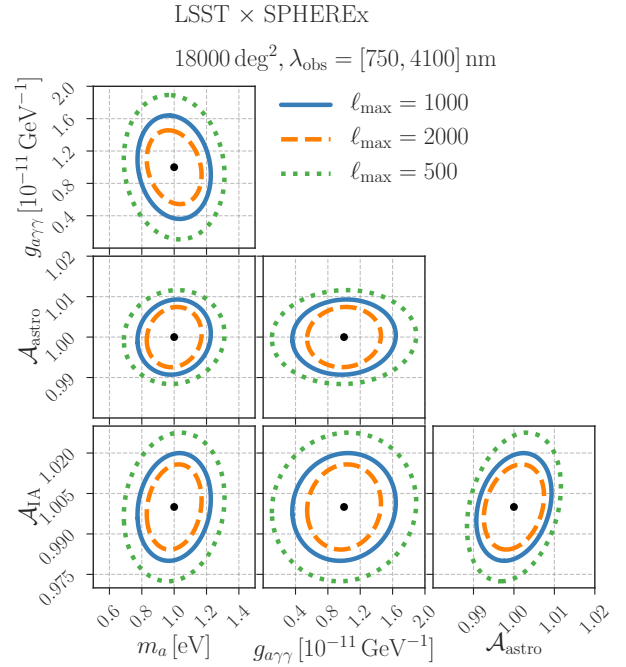


FIG. 7. Forecast of parameter constraints on ALP. In this figure, we assume the cross correlation analysis in hypothetical LSST-like and SPHEREx-like surveys covering 18000 deg^2 . In each panel, the solid error circle represents a 68% confidence level when one uses the cross power spectra at $\ell \leq \ell_{\text{max}} = 1000$. The orange dashed and green dotted lines show the confidence level for $\ell_{\text{max}} = 2000$ and 500 , respectively.

ALP constraints⁹. For reference, our cosmological model predicts

$$k_{\text{max}} = \frac{\ell_{\text{max}}}{\chi(z)} \simeq \left(\frac{\ell_{\text{max}}}{1000} \right) \left(\frac{z}{0.3} \right)^{-1} \left(1 + \frac{z}{2} \right) h\text{Mpc}^{-1}, \quad (53)$$

where k_{max}^{-1} gives an estimate of the smallest physical scale at a fixed ℓ_{max} and redshift z . Eq. (53) has a 10%-level accuracy in the range of $0.05 \leq z \leq 2$. Hence, the power spectrum with $\ell_{\text{max}} = 1000$ can extract the information of structures at $z = 0.3 - 0.4$ with their size of $\gtrsim \text{Mpc}$.

In our analysis, we use multi-frequency information of line intensity maps, allowing us to study the redshift evolution in our cross power spectra. Because the effective redshift in the ALP-decay signal is different from

⁹ It would be worth noting that our theoretical model of cross power spectra is still phenomenological and model uncertainties at small scales are not fully understood yet. Hence, the analysis with larger ℓ_{max} will provide more stringent constraints, while it may induce some biased estimations of the ALP parameters in actual observations.

	Optimistic ($\ell_{\max} = 1000$)	Optimistic ($\ell_{\max} = 2000$)	Pessimistic ($\ell_{\max} = 1000$)	Pessimistic ($\ell_{\max} = 2000$)
Δm_a (eV)	0.150 (0.146)	0.112 (0.107)	0.183 (0.146)	0.146 (0.107)
$\Delta g_{a\gamma\gamma}$ (10^{-11} GeV $^{-1}$)	0.423 (0.416)	0.302 (0.292)	0.672 (0.416)	0.552 (0.292)
$\Delta \mathcal{A}_{\text{astro}} \times 10^3$	6.15 (5.93)	4.92 (4.74)	10.4 (5.93)	8.27 (4.74)
$\Delta \eta_{\text{astro}}$	-	-	0.0301 (0.0171)	0.0191 (0.00904)
$\Delta \mathcal{A}_{\text{IA}} \times 10^2$	1.32 (1.26)	1.04 (0.993)	8.32 (1.26)	6.99 (0.993)
$\Delta \eta_{\text{IA}}$	-	-	0.110 (0.0169)	0.0924 (0.0131)

TABLE II. Summary of the Fisher forecast of the ALP and astrophysics by the cross power spectra between line intensity and weak lensing maps. We assume the effective survey area to be $18,000 \text{ deg}^2$. We consider the LSST-like source galaxy distribution (Eq. [26]) and the intensity maps at $\lambda_{\text{obs}} = 750 - 4100 \text{ nm}$ with the frequency resolution being 41.5. We refer the “optimistic” scenario when the redshift evolution in the astrophysical line intensity and the IA effects are precisely known in advance (i.e. η_{astro} and η_{IA} are fixed). On the other hand, the pessimistic scenario assumes that η_{astro} and η_{IA} are unknown. In each table cell, the number without brackets show the 1σ constraint of single parameter when we marginalize other parameters, while the one in brackets is the un-marginalized counterpart. Note that the fiducial parameters are set to $(m_a, g_{a\gamma\gamma}, \mathcal{A}_{\text{astro}}, \eta_{\text{astro}}, \mathcal{A}_{\text{IA}}, \eta_{\text{IA}}) = (1 \text{ eV}, 1 \times 10^{-11} \text{ GeV}^{-1}, 1, 0, 1, 3)$.

the astrophysical counterparts, the multi-frequency information plays an essential role in breaking degeneracies among our cross power spectra. Nevertheless, we expect that the efficiency of multi-frequency cross correlation depends on our prior knowledge of the redshift evolution in astrophysics-related parts. In our case, the redshift evolution in the astrophysical line intensity and the IA effects of galaxy shapes controls how the multi-frequency analysis works. To see impacts of prior knowledge in the redshift evolution, we consider two scenarios. One is the optimistic scenario when we assume that the parameters of η_{astro} and η_{IA} are perfectly known, and another is the pessimistic scenario making these two parameters unknown. In realistic situations, we will have some informative prior of these two parameters from other analyses. For instance, tomographic cosmic shear analyses can place reasonable constraints of η_{IA} , while analyses of line intensity maps with the SPHEREx deep survey mode provide cleaner information of astrophysical sources and allow us to put constraints of η_{astro} . Hence, our Fisher analysis sets two extreme cases in the cross correlation analysis and gives some sense of how tight constraints of the ALP parameters will be obtained in more realistic situations.

Fig. 7 summarizes an expected constraint in two-dimensional planes for the optimistic scenario with different ℓ_{\max} . We find that the multi-frequency information can successfully break degeneracies among the ALP-decay and astrophysical signals if we precisely know the redshift evolution in the astrophysical signals. Note that cross correlation analyses at single frequencies can not separate the terms of $C_{\text{ALP}-\kappa}$ and $C_{\text{ALP}-\text{IA}}$ in practice. The multi-frequency information can give tight constraints of \mathcal{A}_{IA} as well as $\mathcal{A}_{\text{astro}}$, improving the ALP constraints. Note that the astrophysical-line terms will probe higher-redshift structures than the ALP-decay terms do. This can be seen from the difference in ℓ -dependence of each term. Using larger ℓ_{\max} will help to constrain the ℓ -dependence of the observed power spectra, making the parameter constraints tighter.

For the pessimistic scenario, the parameter degener-

acy between \mathcal{A}_{IA} and η_{IA} is significant as shown in Appendix C (see Fig. 9). This strong degeneracy can degrade the constraints of the ALP parameters by a factor of ~ 1.5 . We expect that the degeneracy between \mathcal{A}_{IA} and η_{IA} can be partly broken if we further apply a tomographic analysis in lensing observables [51], while we leave it for future studies. Table II provides a summary of our Fisher analysis.

V. CONCLUSION AND DISCUSSIONS

In this paper, we have studied cross correlation functions between line intensity and weak lensing maps to search for decaying axion-like particles (ALPs). The ALP decay introduces an emission line with its frequency given by $\nu_a = 1.21 \times 10^{14} (m_a/1 \text{ eV}) \text{ Hz}$, where m_a is the particle mass of ALPs. If a fraction of cosmic dark matter is made up of the ALPs, higher mass-density regions in the universe can emit larger line intensity by the ALP decay, as well as induce a more prominent distortion of background galaxy shapes by gravitational lensing effects. We explored correlation signals caused by the ALP decay and weak gravitational lensing effects in large scale structures. For this purpose, we developed a theoretical framework to predict the cross correlation functions by taking into account several astrophysical lines and intrinsic alignments (IAs) of galaxy shapes. Suppose that the ALP explains the whole abundance of dark matter, our findings are summarized as follows.

- Our baseline model shows that the cross correlation with an eV-mass ALP decay and weak lensing effects can dominate the astrophysical-line counterparts when observed wavelengths are set to $\lambda_{\text{obs}} \sim 2000 - 3000 \text{ nm}$. This is because weak lensing effects in modern galaxy surveys can probe the large-scale structures at redshifts of $z = 0.3 - 0.6$, but astrophysical line sources populate higher- z structures and can not introduce significant correlations.
- Assuming upcoming line intensity measurements

by SPHEREx and weak lensing measurements by the Large Survey of Space and Time (LSST), we found that a null detection of the cross correlation can place stringent upper limits of ALP-to-two-photons coupling $g_{a\gamma\gamma} \lesssim 10^{-11} \text{ GeV}^{-1}$ at $m_a = 1 - 3.5 \text{ eV}$. The expected upper limits improve existing constraints by the study of stellar evolution of horizontal branch to red giants [48] by a factor of $\sim 6 - 10$.

- Main systematic effects in our ALP search arise from the correlation between astrophysical lines and the IA effect. This makes the observed correlation signals negative depending on the IA amplitude. We performed a Fisher analysis to study detectability of the ALP-induced signal in the presence of the correlations between IA effects and astrophysical lines. Our Fisher analysis showed that the ALP decay with $m_a = 1 \text{ eV}$ and $g_{a\gamma\gamma} = 10^{-11} \text{ GeV}^{-1}$ can be constrained with a 68% confidence level of $\Delta m_a \sim 0.1 - 0.2 \text{ eV}$ and $\Delta g_{a\gamma\gamma} \sim 0.3 - 0.7 \times 10^{-11} \text{ GeV}^{-1}$ by SPHEREx and LSST. The constraint depends on maximum multipoles in the analysis and prior information about the redshift evolution in astrophysical effects.

The cross correlation between line intensity and weak lensing maps can test various hints of ALP signals reported so far. For example, Ref. [48] analyzed 39 galactic globular clusters and reported that the observed number ratio of stars in horizontal over red giant branch of old stellar clusters differs from an astronomical prediction with a 2σ level. This discrepancy can be interpreted as the existence of the ALP decay with $g_{a\gamma\gamma} = 0.45_{-0.16}^{+0.12} \times 10^{-10} \text{ GeV}^{-1}$, where the error represents a 68% confidence level. Recently, Ref. [52] studied the ALP decay as a potential origin of the anisotropy of the near-infrared background intensity and found that the ALP decay with $m_a = 2.3 - 3 \text{ eV}$ and $g_{a\gamma\gamma} = 1.1 - 1.6 \times 10^{-10} \text{ GeV}^{-1}$ can explain the excess in the observed power spectrum of background intensity at sub-arcmin scales. These hints can be robustly examined by the cross correlation analysis with SPHEREx and LSST.

We expect that our results will provide a guideline of searching for the ALP decay with large-scale structure data. Weak lensing analyses with several source redshift bins can improve constraints of the IA amplitude and offer further improvements of the ALP constraints. Apart from weak lensing measurements in galaxy imaging surveys, there exist several tracers of large scale structures in the universe. Those include number density of galaxies and secondary anisotropies in the cosmic microwave background (CMB) [53]. Spectroscopic observations of galaxies enable us to map the large-scale structure in three-dimensional space, while such maps are known to be a biased tracer of underlying cosmic dark matter [54] and are subject to redshift space distortion effects [55–57]. Among the secondary effects in CMB, gravitational lensing effects in CMB, referred to as CMB lensing, can

provide cosmological information about higher-redshift matter density distributions at $z = 2 - 4$ [58]. The cross correlation with line intensity maps and CMB lensing allows us to place meaningful constraints of astrophysics but may be less sensitive to the ALP decay. Cross correlations among line intensity maps and large-scale structures would be interesting not only for the ALP search but also constraints of cosmological parameters. We leave cosmological applications for our future study.

ACKNOWLEDGMENTS

We thank Naoki Yoshida and Kana Moriwaki for useful comments. This work is supported by MEXT KAKENHI Grant Numbers of 19K14767 and 20H05861. Numerical computations were carried out on Cray XC50 at the Center for Computational Astrophysics in NAOJ.

Appendix A: Auto power spectra in line intensity and weak lensing maps

1. Gaussian covariance of binned power spectra

Let A , B , X , and Y be two-dimensional Gaussian random fields. The estimator of the cross power spectrum between two fields A and B is given by

$$\hat{C}_{AB}(\ell_i) = \frac{1}{N_{\text{mode}}(\ell_i)} \sum_{\boldsymbol{\ell}; \ell \in \ell_i} \tilde{A}(\boldsymbol{\ell}) \tilde{B}(\boldsymbol{\ell}), \quad (\text{A1})$$

where we employ a linear binning in multipoles ℓ with the bin width being $\Delta\ell$, ℓ_i represents the i -th bin of ℓ , and $N_{\text{mode}}(\ell_i)$ is the number of Fourier modes used for the power spectrum estimation at the i -th bin. The number of Fourier modes can be computed as

$$\begin{aligned} N_{\text{mode}}(\ell_i) &= \sum_{\boldsymbol{\ell}; \ell \in \ell_i} 1 \\ &\simeq \frac{2\pi\ell_i \Delta\ell}{(2\pi)^2/\Omega_S} = 2\ell_i \Delta\ell f_{\text{sky}}, \end{aligned} \quad (\text{A2})$$

where Ω_S is the survey area and $f_{\text{sky}} = \Omega_S/(4\pi)$. The ensemble average of Eq. (A1) is equal to its expected value $C_{AB}(\ell_i)$.

We then consider the covariance matrix between two estimators of $\hat{C}_{AB}(\ell_i)$ and $\hat{C}_{XY}(\ell_j)$. The covariance is defined by

$$\begin{aligned} \text{Cov} \left[\hat{C}_{AB}(\ell_i), \hat{C}_{XY}(\ell_j) \right] &= \langle \hat{C}_{AB}(\ell_i) \hat{C}_{XY}(\ell_j) \rangle \\ &\quad - C_{AB}(\ell_i) C_{XY}(\ell_j). \end{aligned} \quad (\text{A3})$$

For the Gaussian fields, it holds that

$$\begin{aligned} \langle \tilde{A}(\boldsymbol{\ell}) \tilde{B}(\boldsymbol{\ell}) \tilde{X}(\boldsymbol{\ell}') \tilde{Y}(\boldsymbol{\ell}') \rangle &= \langle \tilde{A}(\boldsymbol{\ell}) \tilde{B}(\boldsymbol{\ell}) \rangle \langle \tilde{X}(\boldsymbol{\ell}') \tilde{Y}(\boldsymbol{\ell}') \rangle \\ &\quad + \langle \tilde{A}(\boldsymbol{\ell}) \tilde{X}(\boldsymbol{\ell}') \rangle \langle \tilde{B}(\boldsymbol{\ell}) \tilde{Y}(\boldsymbol{\ell}') \rangle \\ &\quad + \langle \tilde{B}(\boldsymbol{\ell}) \tilde{X}(\boldsymbol{\ell}') \rangle \langle \tilde{A}(\boldsymbol{\ell}) \tilde{Y}(\boldsymbol{\ell}') \rangle. \end{aligned} \quad (\text{A4})$$

Note that

$$\begin{aligned}
& \sum_{\ell; \ell \in \ell_i} \sum_{\ell'; \ell' \in \ell_j} \langle \tilde{A}(\ell) \tilde{X}(\ell') \rangle \langle \tilde{B}(\ell) \tilde{Y}(\ell') \rangle \\
&= \delta_{ij}^K \sum_{\ell; \ell \in \ell_i} \langle \tilde{A}(\ell) \tilde{X}(\ell) \rangle \langle \tilde{B}(\ell) \tilde{Y}(\ell) \rangle \\
&= \delta_{ij}^K \sum_{\ell; \ell \in \ell_i} C_{AX}(\ell_i) C_{BY}(\ell_i) \\
&= \delta_{ij}^K N_{\text{mode}}(\ell_i) C_{AX}(\ell_i) C_{BY}(\ell_i), \quad (\text{A5})
\end{aligned}$$

where δ_{ij}^K is the Kronecker delta symbol. Hence, we arrive at

$$\begin{aligned}
& \langle \hat{C}_{AB}(\ell_i) \hat{C}_{XY}(\ell_j) \rangle - C_{AB}(\ell_i) C_{XY}(\ell_j) \\
&= \frac{\delta_{ij}^K}{N_{\text{mode}}(\ell_i)} \left[C_{AX}(\ell_i) C_{BY}(\ell_i) \right. \\
& \quad \left. + C_{BX}(\ell_i) C_{AY}(\ell_i) \right]. \quad (\text{A6})
\end{aligned}$$

If one sets $A(\boldsymbol{\theta}) = I(\boldsymbol{\theta}|\nu)$, $X(\boldsymbol{\theta}) = I(\boldsymbol{\theta}|\nu')$, $B(\boldsymbol{\theta}) = Y(\boldsymbol{\theta}) = \kappa(\boldsymbol{\theta})$ where $I(\boldsymbol{\theta}|\nu)$ is the observed intensity at the frequency ν and $\kappa(\boldsymbol{\theta})$ is the lensing convergence, Eq. (A6) leads to Eq. (45).

2. Each component in Eq. (45)

As in Eq. (45), the covariance matrix for the cross power spectrum $C_{\text{LIM}-\kappa}^{(\text{obs})}(\ell|\nu)$ includes two components of the cross power spectrum between two different intensity maps $C_{\text{LIM}-\text{LIM}}^{(\text{obs})}(\ell|\nu, \nu')$ and the auto power spectrum of the observed lensing field $C_{\kappa-\kappa}^{(\text{obs})}(\ell)$. We here describe our model of these two power spectra.

The cross power spectrum between two different intensity maps can be computed within the halo model as introduced in Section III B 3. Using the Limber approximation, we formally write

$$\begin{aligned}
C_{\text{LIM}-\text{LIM}}^{(\text{obs})}(\ell|\nu, \nu') &= C_{\text{astro-astro}}(\ell|\nu, \nu') \\
&+ C_{\text{astro-ALP}}(\ell|\nu, \nu') \\
&+ C_{\text{ALP-ALP}}(\ell|\nu, \nu') + C_{\text{N}}(\ell|\nu, \nu'), \quad (\text{A7})
\end{aligned}$$

and each term is given by

$$\begin{aligned}
C_{\text{astro-astro}}(\ell|\nu, \nu') &= \sum_{Q, Q'} \int d\chi \frac{W_Q(z|\nu) W_{Q'}(z|\nu')}{\chi^2} \\
&\times \mathcal{A}_{\text{astro}}^2 (1+z)^{2\eta_{\text{astro}}} P_{\text{astro-astro}} \left(\frac{\ell}{\chi}, z \right), \quad (\text{A8})
\end{aligned}$$

$$\begin{aligned}
C_{\text{astro-ALP}}(\ell|\nu, \nu') &= \sum_Q \int d\chi \left(\frac{W_Q(z|\nu) W_{\text{DM}}(z|\nu')}{\chi^2} \right. \\
&\left. + \frac{W_Q(z|\nu') W_{\text{DM}}(z|\nu)}{\chi^2} \right) \mathcal{A}_{\text{astro}} (1+z)^{\eta_{\text{astro}}} \\
&\times \left(\frac{\Omega_{\text{DM}}}{\Omega_{\text{m0}}} \right) P_{\text{astro-m}} \left(\frac{\ell}{\chi}, z \right), \quad (\text{A9})
\end{aligned}$$

$$\begin{aligned}
C_{\text{ALP-ALP}}(\ell|\nu, \nu') &= \int d\chi \frac{W_{\text{DM}}(z|\nu) W_{\text{DM}}(z|\nu')}{\chi^2} \\
&\times \left(\frac{\Omega_{\text{DM}}}{\Omega_{\text{m0}}} \right)^2 P_{\text{m}} \left(\frac{\ell}{\chi}, z \right), \quad (\text{A10})
\end{aligned}$$

$$C_{\text{N}}(\ell|\nu, \nu') = \delta_{\nu\nu'}^K \frac{\sigma_n^2}{n_{\text{pix}}}, \quad (\text{A11})$$

where $Q = \{\text{H}\alpha, [\text{OII}], [\text{OIII}], \text{H}\beta, \text{Ly}\alpha\}$, $P_{\text{astro-astro}}$ is the three-dimensional auto power spectrum of the field δ_{astro} (see Eq. [21]), σ_n is the observational noise in line intensity maps in units of $\text{erg/s/cm}^2/\text{Hz/str}$, and n_{pix} is the number density of pixels in intensity maps. For a given 5σ -limiting AB magnitude m_{lim} per each pixel, σ_n is given by

$$\sigma_n = \frac{10^{-(m_{\text{lim}}+48.60)/2.5}}{5\theta_{\text{pix}}^2} [\text{erg/s/cm}^2/\text{Hz/str}], \quad (\text{A12})$$

where θ_{pix} is the angular size of each pixel. Note that $n_{\text{pix}} = \theta_{\text{pix}}^{-2}$. Within the halo model, we can compute $P_{\text{astro-astro}}$ as

$$\begin{aligned}
P_{\text{astro-astro}}(k, z) &= P_{\text{astro-astro}}^{\text{1h}}(k, z) \\
&+ P_{\text{astro-astro}}^{\text{2h}}(k, z), \quad (\text{A13})
\end{aligned}$$

$$P_{\text{astro-astro}}^{\text{1h}}(k, z) = \mathcal{N}_{\text{astro}}^{-2}(z) \int dM \frac{dn}{dM} \dot{M}_*^2(M, z), \quad (\text{A14})$$

$$\begin{aligned}
P_{\text{astro-astro}}^{\text{2h}}(k, z) &= \left(\mathcal{N}_{\text{astro}}^{-1}(z) \int dM \frac{dn}{dM} b_h(M, z) \dot{M}_*(M, z) \right)^2 \\
&\times P_L(k, z). \quad (\text{A15})
\end{aligned}$$

In practice, the integrand of Eq. (A7) includes the product of delta functions, leading a divergence. Hence, we approximate the integral over χ by a discrete sum such as

$$\begin{aligned}
& \int d\chi \delta_{\text{D}}^{(1)}(\chi - \chi_Q) \delta_{\text{D}}^{(1)}(\chi - \chi_{Q'}) \cdots \\
&\rightarrow \sum_{i=0}^{\infty} \Delta\chi \Theta(\chi_i - \chi_Q |\Delta\chi) \Theta(\chi_i - \chi_{Q'} |\Delta\chi) \cdots \quad (\text{A16})
\end{aligned}$$

where $\chi_i = (i + 1/2) \Delta\chi$, and the function of $\Theta(\chi - \chi_Q |\Delta\chi)$ returns $1/\Delta\chi$ for $|\chi - \chi_Q| \leq \Delta\chi/2$ and zero

otherwise. The width of comoving distance $\Delta\chi$ is set by

$$\Delta\chi = \left[\left(\frac{d\chi}{dz} \right) \Big|_{z_Q} \frac{1+z_Q}{\nu} \Delta\nu \times \left(\frac{d\chi}{dz} \right) \Big|_{z_{Q'}} \frac{1+z_{Q'}}{\nu'} \Delta\nu' \right]^{1/2}, \quad (\text{A17})$$

where $\Delta\nu = \nu/R$, $\Delta\nu' = \nu'/R$, $z_Q = \nu_Q/\nu - 1$, and $z_{Q'} = \nu_{Q'}/\nu' - 1$. Note that ν_Q is the rest-frame frequency for the line Q and R is the frequency resolution in line intensity mapping measurements.

The auto power spectrum of the observed convergence field, $C_{\kappa-\kappa}^{(\text{obs})}(\ell)$, is then given by

$$\begin{aligned} C_{\kappa-\kappa}^{(\text{obs})}(\ell) = & \int d\chi \frac{W_\kappa^2(z)}{\chi^2} P_m\left(\frac{\ell}{\chi}, z\right) \\ & + \int d\chi \frac{2W_\kappa(z)W_{\text{IA}}(z)}{\chi^2} P_m\left(\frac{\ell}{\chi}, z\right) \\ & + \int d\chi \frac{W_{\text{IA}}^2(z)}{\chi^2} P_m\left(\frac{\ell}{\chi}, z\right) \\ & + \frac{\sigma_e^2}{n_g}, \end{aligned} \quad (\text{A18})$$

where σ_e is the intrinsic scatter of galaxy ellipticities per components, and n_g is the mean number density of source galaxies.

Appendix B: Expected upper limits of dark matter lifetime

Fig. 8 provides an expected 2σ upper limit of the dark matter lifetime Γ by the cross power spectrum between line intensity and weak lensing maps in LSST and SPHEREx.

Appendix C: Full two-dimensional error circles in our Fisher analysis

Fig. 9 provides an expected 68%-level confidence level of our six parameters by the cross power spectrum between line intensity and weak lensing maps in LSST and SPHEREx.

- [1] Planck Collaboration, N. Aghanim, Y. Akrami, M. Ashdown, J. Aumont, C. Baccigalupi, M. Ballardini, A. J. Banday, R. B. Barreiro, N. Bartolo, S. Basak, R. Battye, K. Benabed, J. P. Bernard, M. Bersanelli, P. Bielewicz, J. J. Bock, J. R. Bond, J. Borrill, F. R. Bouchet, F. Boulanger, M. Bucher, C. Burigana, R. C. Butler, E. Calabrese, J. F. Cardoso, J. Carron, A. Challinor, H. C. Chiang, J. Chluba, L. P. L. Colombo, C. Combet, D. Contreras, B. P. Crill, F. Cuttaia, P. de Bernardis, G. de Zotti, J. Delabouille, J. M. Delouis, E. Di Valentino, J. M. Diego, O. Doré, M. Douspis, A. Ducout, X. Dupac, S. Dusini, G. Efstathiou, F. Elsner, T. A. Enßlin, H. K. Eriksen, Y. Fantaye, M. Farhang, J. Fergusson, R. Fernandez-Cobos, F. Finelli, F. Forastieri, M. Frailis, A. A. Fraisse, E. Franceschi, A. Frolov, S. Galeotta, S. Galli, K. Ganga, R. T. Génova-Santos, M. Gerbino, T. Ghosh, J. González-Nuevo, K. M. Górski, S. Gratton, A. Gruppuso, J. E. Gudmundsson, J. Hamann, W. Handley, F. K. Hansen, D. Herranz, S. R. Hildebrandt, E. Hivon, Z. Huang, A. H. Jaffe, W. C. Jones, A. Karakci, E. Keihänen, R. Keskitalo, K. Kiiveri, J. Kim, T. S. Kisner, L. Knox, N. Krachmalnicoff, M. Kunz, H. Kurki-Suonio, G. Lagache, J. M. Lamarre, A. Lasenby, M. Lattanzi, C. R. Lawrence, M. Le Jeune, P. Lemos, J. Lesgourgues, F. Levrier, A. Lewis, M. Liguori, P. B. Lilje, M. Lilley, V. Lindholm, M. López-Caniiego, P. M. Lubin, Y. Z. Ma, J. F. Macías-Pérez, G. Maggio, D. Maino, N. Mandolesi, A. Mangilli, A. Marcos-Caballero, M. Maris, P. G. Martin, M. Martinelli, E. Martínez-González, S. Matarrese, N. Mauri, J. D. McEwen, P. R. Meinhold, A. Melchiorri, A. Mennella, M. Migliaccio, M. Mil-

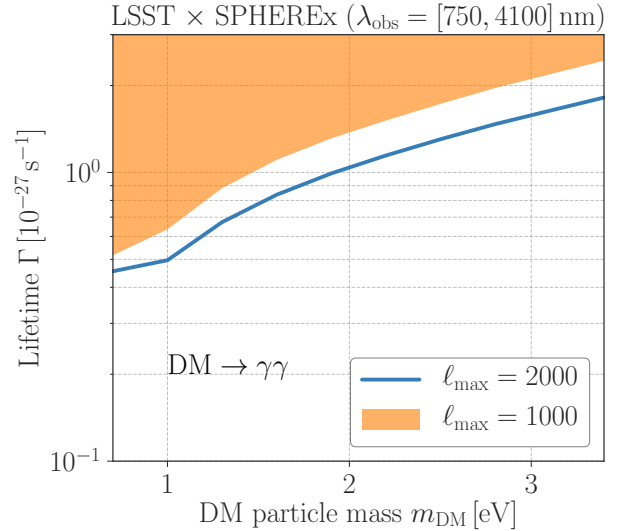


FIG. 8. 2σ -level upper limits of the lifetime of decaying dark matter (DM) Γ as a function of DM mass m_{DM} . The orange shaded region can be excluded by the cross correlation analysis with SPHEREx line intensity maps and LSST lensing when one uses the power spectra with $\ell \leq \ell_{\text{max}} = 1000$. The blue line shows the limits when one uses the information from smaller angular scales with $\ell_{\text{max}} = 2000$.

lea, S. Mitra, M. A. Miville-Deschênes, D. Molinari, L. Montier, G. Morgante, A. Moss, P. Natoli, H. U.

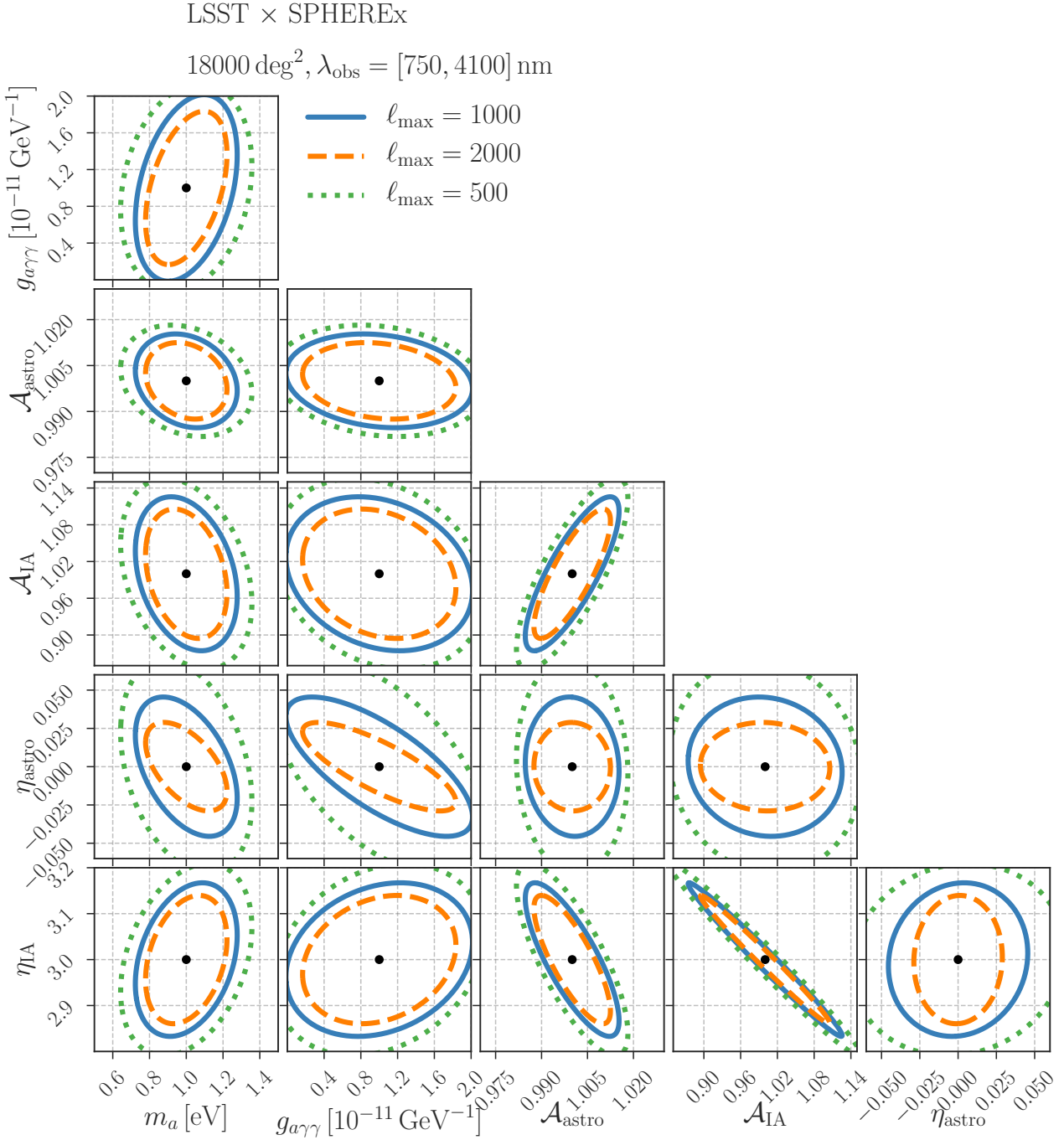


FIG. 9. Similar to Fig. 7, but we include uncertainties of redshift evolution in astrophysical line intensity and intrinsic alignments of galaxy shapes.

Nørgaard-Nielsen, L. Pagano, D. Paoletti, B. Partridge, G. Patanchon, H. V. Peiris, F. Perrotta, V. Pettorino, F. Piacentini, L. Polastri, G. Polenta, J. L. Puget, J. P. Rachen, M. Reinecke, M. Remazeilles, A. Renzi, G. Rocha, C. Rosset, G. Roudier, J. A. Rubiño-Martín, B. Ruiz-Granados, L. Salvati, M. Sandri, M. Savelainen, D. Scott, E. P. S. Shellard, C. Sirignano, G. Sirri, L. D. Spencer, R. Sunyaev, A. S. Suur-Uski, J. A. Tauber,

D. Tavagnacco, M. Tenti, L. Toffolatti, M. Tomasi, T. Trombetti, L. Valenziano, J. Valiviita, B. Van Tent, L. Vibert, P. Vielva, F. Villa, N. Vittorio, B. D. Wandelt, I. K. Wehus, M. White, S. D. M. White, A. Zacchei, and A. Zonca, *A&A* **641**, A6 (2020), arXiv:1807.06209 [astro-ph.CO].

[2] J. Preskill, M. B. Wise, and F. Wilczek, *Physics Letters B* **120**, 127 (1983).

- [3] L. F. Abbott and P. Sikivie, *Physics Letters B* **120**, 133 (1983).
- [4] M. Dine and W. Fischler, *Physics Letters B* **120**, 137 (1983).
- [5] R. D. Peccei and H. R. Quinn, *Phys. Rev. Lett.* **38**, 1440 (1977).
- [6] R. D. Peccei and H. R. Quinn, *Phys. Rev. D* **16**, 1791 (1977).
- [7] F. Wilczek, *Phys. Rev. Lett.* **40**, 279 (1978).
- [8] S. Weinberg, *Phys. Rev. Lett.* **40**, 223 (1978).
- [9] P. Svrcek and E. Witten, *Journal of High Energy Physics* **2006**, 051 (2006), arXiv:hep-th/0605206 [hep-th].
- [10] A. Arvanitaki, S. Dimopoulos, S. Dubovsky, N. Kaloper, and J. March-Russell, *Phys. Rev. D* **81**, 123530 (2010), arXiv:0905.4720 [hep-th].
- [11] P. Arias, D. Cadamuro, M. Goodsell, J. Jaeckel, J. Redondo, and A. Ringwald, *J. Cosmology Astropart. Phys.* **2012**, 013 (2012), arXiv:1201.5902 [hep-ph].
- [12] M. Cicoli, M. D. Goodsell, and A. Ringwald, *Journal of High Energy Physics* **2012**, 146 (2012), arXiv:1206.0819 [hep-th].
- [13] N. Blinov, M. J. Dolan, P. Draper, and J. Kozaczuk, *Phys. Rev. D* **100**, 015049 (2019), arXiv:1905.06952 [hep-ph].
- [14] M. Bartelmann and P. Schneider, *Physics Reports* **340**, 291 (2001).
- [15] C. Creque-Sarbinowski and M. Kamionkowski, *Phys. Rev. D* **98**, 063524 (2018), arXiv:1806.11119 [astro-ph.CO].
- [16] J. L. Bernal, A. Caputo, and M. Kamionkowski, arXiv e-prints, arXiv:2012.00771 (2020), arXiv:2012.00771 [astro-ph.CO].
- [17] J. Kennicutt, Robert C., *ARA&A* **36**, 189 (1998), arXiv:astro-ph/9807187 [astro-ph].
- [18] D. Sobral, I. Smail, P. N. Best, J. E. Geach, Y. Matsuda, J. P. Stott, M. Cirasuolo, and J. Kurk, *Mon. Not. Roy. Astron. Soc.* **428**, 1128 (2013), arXiv:1202.3436 [astro-ph.CO].
- [19] M. B. Silva, S. Zaroubi, R. Kooistra, and A. Cooray, arXiv e-prints, arXiv:1711.09902 (2017), arXiv:1711.09902 [astro-ph.GA].
- [20] P. Anders and U. Fritze-v. Alvensleben, *A&A* **401**, 1063 (2003), arXiv:astro-ph/0302146 [astro-ph].
- [21] E. Mármol-Queraltó, R. J. McLure, F. Cullen, J. S. Dunlop, A. Fontana, and D. J. McLeod, *Mon. Not. Roy. Astron. Soc.* **460**, 3587 (2016), arXiv:1511.01911 [astro-ph.GA].
- [22] C. Ly, M. A. Malkan, N. Kashikawa, K. Shimasaku, M. Doi, T. Nagao, M. Iye, T. Kodama, T. Morokuma, and K. Motohara, *ApJ* **657**, 738 (2007), arXiv:astro-ph/0610846 [astro-ph].
- [23] A. A. Khostovan, D. Sobral, B. Mobasher, P. N. Best, I. Smail, J. P. Stott, S. Hemmati, and H. Nayyeri, *Mon. Not. Roy. Astron. Soc.* **452**, 3948 (2015), arXiv:1503.00004 [astro-ph.GA].
- [24] D. Calzetti, L. Armus, R. C. Bohlin, A. L. Kinney, J. Koornneef, and T. Storchi-Bergmann, *ApJ* **533**, 682 (2000), arXiv:astro-ph/9911459 [astro-ph].
- [25] N. Scoville, A. Faisst, P. Capak, Y. Kakazu, G. Li, and C. Steinhardt, *ApJ* **800**, 108 (2015), arXiv:1412.8219 [astro-ph.GA].
- [26] M. Hayashi, D. Sobral, P. N. Best, I. Smail, and T. Kodama, *Mon. Not. Roy. Astron. Soc.* **430**, 1042 (2013), arXiv:1212.4905 [astro-ph.CO].
- [27] C. Chang, M. Jarvis, B. Jain, S. M. Kahn, D. Kirkby, A. Connolly, S. Krughoff, E. H. Peng, and J. R. Peterson, *Mon. Not. Roy. Astron. Soc.* **434**, 2121 (2013), arXiv:1305.0793 [astro-ph.CO].
- [28] M. J. West, J. V. Villumsen, and A. Dekel, *ApJ* **369**, 287 (1991).
- [29] G. Tormen, *Mon. Not. Roy. Astron. Soc.* **290**, 411 (1997), arXiv:astro-ph/9611078 [astro-ph].
- [30] M. A. Troxel and M. Ishak, *Phys. Rep.* **558**, 1 (2015), arXiv:1407.6990 [astro-ph.CO].
- [31] P. Catelan, M. Kamionkowski, and R. D. Blandford, *Mon. Not. Roy. Astron. Soc.* **320**, L7 (2001), arXiv:astro-ph/0005470 [astro-ph].
- [32] C. M. Hirata and U. Seljak, *Phys. Rev. D* **70**, 063526 (2004), arXiv:astro-ph/0406275 [astro-ph].
- [33] J. Fluri, T. Kacprzak, A. Lucchi, A. Refregier, A. Amara, T. Hofmann, and A. Schneider, *Phys. Rev. D* **100**, 063514 (2019), arXiv:1906.03156 [astro-ph.CO].
- [34] M. L. Brown, A. N. Taylor, N. C. Hambly, and S. Dye, *Mon. Not. Roy. Astron. Soc.* **333**, 501 (2002), arXiv:astro-ph/0009499 [astro-ph].
- [35] C. Hikage, M. Oguri, T. Hamana, S. More, R. Mandelbaum, M. Takada, F. Köhlinger, H. Miyatake, A. J. Nishizawa, H. Aihara, R. Armstrong, J. Bosch, J. Coupon, A. Ducout, P. Ho, B.-C. Hsieh, Y. Komiyama, F. Lanusse, A. Leauthaud, R. H. Lupton, E. Medezinski, S. Mineo, S. Miyama, S. Miyazaki, R. Murata, H. Murayama, M. Shirasaki, C. Sifón, M. Simet, J. Speagle, D. N. Spergel, M. A. Strauss, N. Sugiyama, M. Tanaka, Y. Utsumi, S.-Y. Wang, and Y. Yamada, *PASJ* **71**, 43 (2019), arXiv:1809.09148 [astro-ph.CO].
- [36] M. A. Troxel, N. MacCrann, J. Zuntz, T. F. Eifler, E. Krause, S. Dodelson, D. Gruen, J. Blazek, O. Friedrich, S. Samuroff, J. Prat, L. F. Secco, C. Davis, A. Ferté, J. DeRose, A. Alarcon, A. Amara, E. Baxter, M. R. Becker, G. M. Bernstein, S. L. Bridle, R. Cawthon, C. Chang, A. Choi, J. De Vicente, A. Drlica-Wagner, J. Elvin-Poole, J. Frieman, M. Gatti, W. G. Hartley, K. Honscheid, B. Hoyle, E. M. Huff, D. Huterer, B. Jain, M. Jarvis, T. Kacprzak, D. Kirk, N. Kokron, C. Krawiec, O. Lahav, A. R. Liddle, J. Peacock, M. M. Rau, A. Refregier, R. P. Rollins, E. Rozo, E. S. Rykoff, C. Sánchez, I. Sevilla-Noarbe, E. Sheldon, A. Stebbins, T. N. Varga, P. Vielzeuf, M. Wang, R. H. Wechsler, B. Yanny, T. M. C. Abbott, F. B. Abdalla, S. Allam, J. Annis, K. Bechtol, A. Benoit-Lévy, E. Bertin, D. Brooks, E. Buckley-Geer, D. L. Burke, A. Carnero Rosell, M. Carrasco Kind, J. Carretero, F. J. Castander, M. Crocce, C. E. Cunha, C. B. D'Andrea, L. N. da Costa, D. L. DePoy, S. Desai, H. T. Diehl, J. P. Dietrich, P. Doel, E. Fernandez, B. Flaugher, P. Fosalba, J. García-Bellido, E. Gaztanaga, D. W. Gerdes, T. Giannantonio, D. A. Goldstein, R. A. Gruendl, J. Gschwend, G. Gutierrez, D. J. James, T. Jeltema, M. W. G. Johnson, M. D. Johnson, S. Kent, K. Kuehn, S. Kuhlmann, N. Kuropatkin, T. S. Li, M. Lima, H. Lin, M. A. G. Maia, M. March, J. L. Marshall, P. Martini, P. Melchior, F. Menanteau, R. Miquel, J. J. Mohr, E. Neilsen, R. C. Nichol, B. Nord, D. Petravick, A. A. Plazas, A. K. Romer, A. Roodman, M. Sako, E. Sanchez, V. Scarpine, R. Schindler, M. Schubnell, M. Smith, R. C. Smith, M. Soares-Santos, F. Sobreira, E. Suchyta, M. E. C. Swanson, G. Tarle, D. Thomas, D. L. Tucker, V. Vikram, A. R. Walker, J. Weller, Y. Zhang, and DES Collaboration, *Phys. Rev. D* **98**,

- 043528 (2018), arXiv:1708.01538 [astro-ph.CO].
- [37] T. Hamana, M. Shirasaki, S. Miyazaki, C. Hikage, M. Oguri, S. More, R. Armstrong, A. Leauthaud, R. Mandelbaum, H. Miyatake, A. J. Nishizawa, M. Simet, M. Takada, H. Aihara, J. Bosch, Y. Komiyama, R. Lupton, H. Murayama, M. A. Strauss, and M. Tanaka, *PASJ* **72**, 16 (2020), arXiv:1906.06041 [astro-ph.CO].
- [38] O. Doré, J. Bock, M. Ashby, P. Capak, A. Cooray, R. de Putter, T. Eifler, N. Flagey, Y. Gong, S. Habib, K. Heitmann, C. Hirata, W.-S. Jeong, R. Katti, P. Korngut, E. Krause, D.-H. Lee, D. Masters, P. Mausekopf, G. Melnick, B. Mennesson, H. Nguyen, K. Öberg, A. Pullen, A. Raccanelli, R. Smith, Y.-S. Song, V. Tolls, S. Unwin, T. Venumadhav, M. Viero, M. Werner, and M. Zemcov, arXiv e-prints, arXiv:1412.4872 (2014), arXiv:1412.4872 [astro-ph.CO].
- [39] D. N. Limber, *ApJ* **119**, 655 (1954).
- [40] R. Takahashi, M. Sato, T. Nishimichi, A. Taruya, and M. Oguri, *ApJ* **761**, 152 (2012), arXiv:1208.2701 [astro-ph.CO].
- [41] N. E. Chisari, A. J. Mead, S. Joudaki, P. G. Ferreira, A. Schneider, J. Mohr, T. Tröster, D. Alonso, I. G. McCarthy, S. Martin-Alvarez, J. Devriendt, A. Slyz, and M. P. van Daalen, *The Open Journal of Astrophysics* **2**, 4 (2019), arXiv:1905.06082 [astro-ph.CO].
- [42] A. Cooray and R. Sheth, *Phys. Rep.* **372**, 1 (2002), arXiv:astro-ph/0206508 [astro-ph].
- [43] J. F. Navarro, C. S. Frenk, and S. D. M. White, *ApJ* **462**, 563 (1996), arXiv:astro-ph/9508025 [astro-ph].
- [44] B. Diemer and A. V. Kravtsov, *ApJ* **799**, 108 (2015), arXiv:1407.4730 [astro-ph.CO].
- [45] J. Tinker, A. V. Kravtsov, A. Klypin, K. Abazajian, M. Warren, G. Yepes, S. Gottlöber, and D. E. Holz, *ApJ* **688**, 709 (2008), arXiv:0803.2706 [astro-ph].
- [46] J. L. Tinker, B. E. Robertson, A. V. Kravtsov, A. Klypin, M. S. Warren, G. Yepes, and S. Gottlöber, *ApJ* **724**, 878 (2010), arXiv:1001.3162 [astro-ph.CO].
- [47] Q. Guo, S. White, R. E. Angulo, B. Henriques, G. Lemson, M. Boylan-Kolchin, P. Thomas, and C. Short, *Mon. Not. Roy. Astron. Soc.* **428**, 1351 (2013), arXiv:1206.0052 [astro-ph.CO].
- [48] A. Ayala, I. Domínguez, M. Giannotti, A. Mirizzi, and O. Straniero, *Phys. Rev. Lett.* **113**, 191302 (2014), arXiv:1406.6053 [astro-ph.SR].
- [49] M. Arik, S. Aune, K. Barth, A. Belov, S. Borghi, H. Bräuninger, G. Cantatore, J. M. Carmona, S. A. Cetin, J. I. Collar, E. Da Riva, T. Dafni, M. Davenport, C. Eleftheriadis, N. Elias, G. Fanourakis, E. Ferrer-Ribas, P. Friedrich, J. Galán, J. A. García, A. Gardikiotis, J. G. Garza, E. N. Gazis, T. Gerasis, E. Georgiopolou, I. Giomataris, S. Gninenko, H. Gómez, M. Gómez Marzoa, E. Gruber, T. Guthörl, R. Hartmann, S. Hauf, F. Haug, M. D. Hasinoff, D. H. H. Hoffmann, F. J. Iguaz, I. G. Irastorza, J. Jacoby, K. Jakovčić, M. Karuza, K. Königsmann, R. Kotthaus, M. Krčmar, M. Kuster, B. Lakić, P. M. Lang, J. M. Laurent, A. Liolios, A. Ljubičić, G. Luzón, S. Neff, T. Niinikoski, A. Nordt, T. Papaevangelou, M. J. Pivovarov, G. Raffelt, H. Riege, A. Rodríguez, M. Rosu, J. Ruz, I. Savvidis, I. Shilon, P. S. Silva, S. K. Solanki, L. Stewart, A. Tomás, M. Tsagri, K. van Bibber, T. Vafeiadis, J. Villar, J. K. Vogel, S. C. Yildiz, K. Zioutas, and CAST Collaboration, *Phys. Rev. Lett.* **112**, 091302 (2014), arXiv:1307.1985 [hep-ex].
- [50] M. Regis, M. Taoso, D. Vaz, J. Brinchmann, S. L. Zoutendijk, N. Bouché, and M. Steinmetz, arXiv e-prints, arXiv:2009.01310 (2020), arXiv:2009.01310 [astro-ph.CO].
- [51] W. Hu, *ApJ* **522**, L21 (1999), arXiv:astro-ph/9904153 [astro-ph].
- [52] A. Caputo, A. Vittino, N. Fornengo, M. Regis, and M. Taoso, arXiv e-prints, arXiv:2012.09179 (2020), arXiv:2012.09179 [astro-ph.CO].
- [53] N. Aghanim, S. Majumdar, and J. Silk, *Reports on Progress in Physics* **71**, 066902 (2008), arXiv:0711.0518 [astro-ph].
- [54] V. Desjacques, D. Jeong, and F. Schmidt, *Phys. Rep.* **733**, 1 (2018), arXiv:1611.09787 [astro-ph.CO].
- [55] P. J. E. Peebles, *The large-scale structure of the universe* (1980).
- [56] A. J. S. Hamilton, Linear Redshift Distortions: a Review, in *The Evolving Universe*, Vol. 231, edited by D. Hamilton (1998) p. 185.
- [57] R. Scoccimarro, *Phys. Rev. D* **70**, 083007 (2004), arXiv:astro-ph/0407214 [astro-ph].
- [58] A. Lewis and A. Challinor, *Phys. Rep.* **429**, 1 (2006), arXiv:astro-ph/0601594 [astro-ph].